

NOTE TO USERS

This reproduction is the best copy available.

UMI[®]

Hemodynamics of an Anatomically Realistic Human Aorta

Youssef Biadillah

Mechanical Engineering
McGill University, Montreal

May, 2005

A thesis submitted to McGill University in partial fulfillment of the
requirements of the degree of Masters of Engineering

© Youssef Biadillah, 2005



Library and
Archives Canada

Bibliothèque et
Archives Canada

Published Heritage
Branch

Direction du
Patrimoine de l'édition

395 Wellington Street
Ottawa ON K1A 0N4
Canada

395, rue Wellington
Ottawa ON K1A 0N4
Canada

Your file *Votre référence*

ISBN: 0-494-12584-5

Our file *Notre référence*

ISBN: 0-494-12584-5

NOTICE:

The author has granted a non-exclusive license allowing Library and Archives Canada to reproduce, publish, archive, preserve, conserve, communicate to the public by telecommunication or on the Internet, loan, distribute and sell theses worldwide, for commercial or non-commercial purposes, in microform, paper, electronic and/or any other formats.

The author retains copyright ownership and moral rights in this thesis. Neither the thesis nor substantial extracts from it may be printed or otherwise reproduced without the author's permission.

AVIS:

L'auteur a accordé une licence non exclusive permettant à la Bibliothèque et Archives Canada de reproduire, publier, archiver, sauvegarder, conserver, transmettre au public par télécommunication ou par l'Internet, prêter, distribuer et vendre des thèses partout dans le monde, à des fins commerciales ou autres, sur support microforme, papier, électronique et/ou autres formats.

L'auteur conserve la propriété du droit d'auteur et des droits moraux qui protègent cette thèse. Ni la thèse ni des extraits substantiels de celle-ci ne doivent être imprimés ou autrement reproduits sans son autorisation.

In compliance with the Canadian Privacy Act some supporting forms may have been removed from this thesis.

Conformément à la loi canadienne sur la protection de la vie privée, quelques formulaires secondaires ont été enlevés de cette thèse.

While these forms may be included in the document page count, their removal does not represent any loss of content from the thesis.

Bien que ces formulaires aient inclus dans la pagination, il n'y aura aucun contenu manquant.


Canada

Acknowledgments

I would like to thank both Dr. Rosaire Mongrain and Dr. Richard Leask for their support and guidance during my time at McGill. I want to thank my parents Dr. Mohamed Cheikh Biadillah and Jamila Chenguiti for their never ending love and support. I want to thank my dear friend Isam Faik for his guidance and help all the way from high school until today and my colleagues Adrian, Heidi, Nushi, Neil and Tin. Last but not least Lea, Magali, and Youssef: Thank you for your friendship, and keeping up with my crazy mind.

Abstract

Cardiovascular disease (CVD) is North America's leading killer for both men and women among all racial and ethnic groups. Almost 1 million North Americans die of CVD each year, which adds up to 42% of all deaths.

Numerous investigations point out that normal blood flow (hemodynamics) is essential to good health and many studies found that there is a relationship between the genesis and the progression of CVD with the locally irregular blood flow occurring in the diseased zones.

The study of hemodynamics in the cardiovascular system is therefore key to the understanding of CVD; its genesis and progression.

The aorta is the largest artery in the body, rising from the heart's major pumping chamber, the left ventricle. It is the primary artery of the circulatory system, delivering oxygenated blood to all other arteries except those of the lungs and is a major site for CVD.

Despite the clinical importance of the aorta, relatively little is known about its hemodynamic features due in part to the difficulty of studying blood flow in this artery.

This thesis presents a numerical analysis on the hemodynamics of a 3D realistic model of the human aorta and its arch reconstructed from Magnetic Resonance Imaging (MRI) data.

The objective was to evaluate the effect of flow waveform and inlet flow velocity profile on the hemodynamics in the proximal, medial, distal regions of the aorta and on the hemodynamics in the branches.

Résumé

Les maladies cardiovasculaires représentent la première cause de mortalité en Amérique du Nord toute catégorie d'âge et d'ethnicité confondue. A peu près un million de nord-américains en meurent chaque année, ce qui représentent 42% des mortalités annuelles. Plusieurs études ont démontré qu'un écoulement sanguin normal est essentiel pour maintenir une personne en bonne santé et plusieurs autres études ont démontré qu'il y a un lien très fort entre la naissance et la progression des maladies cardiovasculaires et l'écoulement sanguin irrégulier dans les zones affectées. Il est donc impératif d'étudier l'écoulement dans le système cardiovasculaire pour une meilleure compréhension des maladies cardiovasculaires : leur initiation et progression.

L'aorte est la plus grosse artère du corps humain, elle prend origine au niveau du ventricule gauche : la plus importante chambre génératrice de pression dans le cœur humain.

L'aorte est la plus importante artère dans le système cardiovasculaire et délivre le sang riche en oxygène à toutes les autres artères du corps humain, elle est aussi un site très souvent affecté par les maladies cardiovasculaires.

Même si l'aorte a une importance clinique très importante, peu d'études ont été entreprises pour étudier son écoulement sanguin caractéristique, cela est dû en parti à la complexité de la géométrie à étudier.

Cette thèse présente une étude numérique de l'écoulement sanguin caractéristique d'un modèle réaliste d'une aorte humaine reconstruite à partir de données de résonance magnétiques. L'objectif étant d'évaluer l'effet des conditions limites de l'écoulement sanguin à l'entrée de l'aorte sur les résultats de l'écoulement sanguin, les distributions de vitesse, de pression, et de cisaillements dans les parties distales de l'aorte et des branches aortiques.

CHAPTER 1: INTRODUCTION	1
CHAPTER 2: LITERATURE REVIEW	2
2.1 THE AORTA	2
2.2 MEDICAL CONTEXT	3
2.2.1 <i>Atherosclerosis</i>	3
2.2.2 <i>Aortic Aneurysm</i>	4
2.2.3 <i>Aortic Dissection</i> :.....	6
2.2.4 <i>Coarctation of the Aorta</i> :	7
2.3 HEMODYNAMICS.....	8
2.3.1 <i>Idealized Flow Models</i>	9
2.3.2 <i>Cardiovascular Disease and Blood Flow</i>	12
2.3.3 <i>Blood Flow in Simple Anatomical Geometries</i>	14
2.3.4 <i>Blood Flow in Aortic Models</i>	15
CHAPTER 3: METHODOLOGY	18
3.1 OVERVIEW	18
3.2 DATA ACQUISITION USING MAGNETIC RESONANCE IMAGING	19
3.3 3D RECONSTRUCTION USING 3D DOCTOR	21
3.4 GLOBAL SURFACE CORRECTIONS USING PRO ENGINEER:	23
3.5 MESH GENERATION USING ICEM/CFD:	25
3.6 NUMERICAL ANALYSIS USING ANSYS FLOTTRAN.....	27
3.7 POST PROCESSING USING TECPLOT	28
3.8 GOVERNING EQUATIONS AND BOUNDARY CONDITIONS	30
3.8.1 <i>Governing Equations</i>	30
3.8.2 <i>Blood Properties</i>	30
3.8.3 <i>Boundary Conditions</i>	31
3.9 MESH INDEPENDENCE VALIDATION.....	32
CHAPTER 4: FLOW HEMODYNAMICS IN THE AORTIC ARCH	37
4.1 FLOW DISTRIBUTION INTO THE BRANCHES	37
4.2 FLOW VELOCITY RESULTS.....	38
4.2.1 <i>Overview</i>	38
4.2.2 <i>Velocity Results</i>	40
4.3 PRESSURE RESULTS	52
4.4 SHEAR RESULTS	54
4.5 DISCUSSION	59
4.6 STUDY LIMITATIONS.....	63
CHAPTER 5: EFFECTS OF INLET FLOW CONDITIONS ON FLOW RESULTS	64
5.1 INLET FLOW CONDITIONS IN THE ASCENDING AORTA	64
5.2 INFLUENCE OF INLET BOUNDARY CONDITIONS ON VELOCITY RESULTS	65
5.2.1 <i>Overview</i>	65
5.2.2 <i>Velocity Results</i>	67
5.3 EFFECT OF INLET BOUNDARY CONDITIONS ON FLOW DISTRIBUTION INTO THE BRANCHES	79
5.4 INFLUENCE OF INLET BOUNDARY CONDITIONS ON PRESSURE RESULTS	80
5.5 INFLUENCE OF INLET BOUNDARY CONDITIONS ON SHEAR RESULTS.....	83
5.6 DISCUSSION	86
5.7 STUDY LIMITATIONS.....	88
CHAPTER 6: CONTRIBUTIONS AND CONCLUSIONS	89
REFERENCES	91

Chapter 1: Introduction

The aorta is the primary artery of the circulatory system, delivering oxygenated blood to all other arteries except those of the lungs and is a major site for arterial disease. Despite the clinical importance of the aorta, relatively little is known about its hemodynamic features due in part to the difficulty of studying blood flow in this artery.

Most studies in hemodynamics have focused instead on coronary arteries, abdominal aortas, carotid bifurcations, and cerebral arteries using realistic models or simplified geometries such as bifurcations and curved tubes. Recently, however, numerical and experimental studies have been performed using realistic models of three dimensional reconstructions of aortic arches including the aortic branches.

This study is a continuation of the recent efforts in elucidating blood flow patterns in the human aortic arch and presents a numerical analysis on the hemodynamics of the aorta with a focus on velocity, pressure, and shear stress distributions. The objective was to evaluate the effect of flow waveform and inlet flow velocity profile on the hemodynamics in the proximal, medial, distal regions of the aorta and on the hemodynamics in the branches.

The major hypothesis was that the hemodynamics downstream of the aorta is mainly dictated by its complex geometry and that inlet flow conditions will have little influence on the hemodynamics within the branches and the distal part of the aorta.

The findings of the study should help medical practitioners better understand the hemodynamics in the aorta, correlate it with aortic disease genesis and progression, and design better therapies and disease management strategies. In addition, a better understanding of the hemodynamics should help medical device designers improve devices used in interventions related to aortic disease treatment.

Chapter 2: Literature Review

2.1 The Aorta

The aorta is the largest artery in the body, rising from the heart's major pumping chamber, the left ventricle. Oxygen-rich blood enters the aorta with each contraction of the left ventricle and travels throughout the body through the smaller arteries branching from it. Figure 2.1 illustrates a healthy human aorta with its main anatomic features:

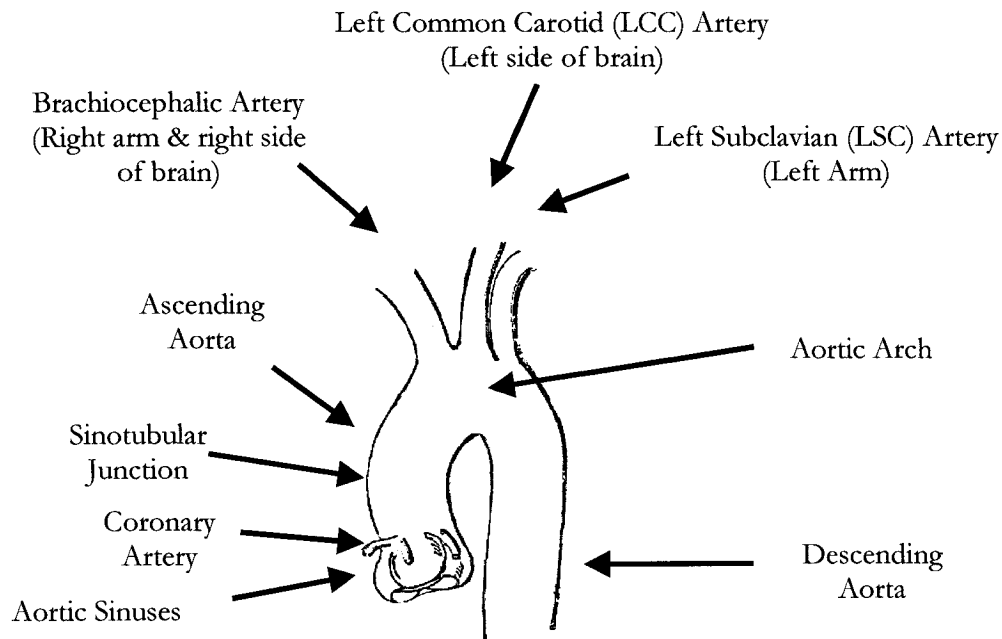


Figure 2.1 Illustration showing the main features of the human aorta

The aortic root is the beginning of the aorta. Starting from the aortic valve (annulus) and becoming slightly wider in diameter (sinuses of Valsalva), it gives rise to two coronary arteries and ends at the beginning of the ascending aorta (sinotubular junction). The two coronary arteries are responsible for carrying oxygen-rich blood to the heart muscle itself.

The ascending aorta extends upward from the aortic root to the point where the innominate artery branches off the aorta, and the aorta begins to form an arch. At

this level, the aorta gets little support from surrounding tissue and must face the entire cardiac output volume (minus the coronary arteries), making the ascending segment a vulnerable part of the aorta to aneurysm formation, dissection and rupture.

The aortic arch represents the curved portion at the top of the aorta. The brachiocephalic, left common carotid, and left subclavian arteries, which supply blood to the head and upper body, branch from the arch. It is outside the pericardial sack and generally has better support from surrounding structures.

2.2 Medical Context

Cardiovascular disease is North America's leading killer for both men and women among all racial and ethnic groups. Almost 1 million North Americans die of CVD each year, which adds up to 42% of all deaths (American Heart Association, 2005).

The aorta is often implicated in cardiovascular disease, its causes are various and include smoking, trauma, connective tissue disorder, and hypertension and it takes different forms: The result is atherosclerosis, aneurysm formations, and dissections.

2.2.1 Atherosclerosis

Atherosclerosis comes from the Greek words athero, meaning gruel or paste, and sclerosis, meaning hardness. It is a gradual process that occurs when cholesterol collects under the inner lining of artery walls. These cholesterol deposits eventually may result in fibrosis and calcification which result in hardening of the tissue. Atherosclerosis may narrow or block the artery and hinder blood flow; it may lead to wall remodeling, rupture, and or dissection. It begins at the inner layer of the arterial wall, at the point where deposition of lipids, mainly cholesterol, occurs; at the endothelial layer itself or within the intima. Many studies have tried to explain the etiology of atherosclerosis; these have been discussed by Constantinides (1965). One of the theories is lipid filtration which presents atherosclerotic lesions as a reaction of the arterial wall against lipids which invade it from the blood stream. The principal factors involved in this phenomenon are considered to be: changes in the chemical

composition of the blood, changes in the structure of the arterial wall, the fluid flow distributions which may bring the rich in lipids fluid streams into contact with the arterial wall. One of the basic features of atherosclerosis is that it occurs predominantly at specific sites of the arterial system. It seems therefore appropriate to consider its association with the blood flow phenomena, which are implicated here in the etiology. The development of atherosclerosis *in vivo* occurs preferentially at arterial locations such as bifurcations and regions of high curvature that exhibit disturbed blood flow (Davies *et al.* 1997). Endothelial cells (ECs), which are cells of the endothelium the inner layer of the arterial wall, adapt to this hemodynamic environment both structurally and functionally, and endothelial dysfunction in these regions is sometimes associated with inflammatory processes responsible for atherosclerosis (Ross 1995). Davies *et al.* (1997) found that biochemical signaling is rapidly initiated at multiple locations within ECs following alterations in the fluid shear stress profile acting at the cell surface. The mechanisms, by which ECs sense changes in hemodynamics and transduce mechanical stimuli into biomechanical signaling, have and are still, being studied.

2.2.2 Aortic Aneurysm

The permanent enlargement of some portion of a blood vessel is often described as bulging, ballooning or dilated. The diameter of the enlargement will determine whether or not it is considered an aneurysm. Traditionally for the aorta, any permanently dilated section measuring 4.0 cm or greater in diameter has been called an aneurysm (Heart Center, 2004).

The definition of an aneurysm may also be based on comparison with the normal blood vessel size for an individual. When the permanent enlargement of some part of a blood vessel is at least 1.5 times greater than normal size, it may be termed an aneurysm. Applying this to the aorta, if an individual's normal aorta is 2.5 cm, then dilation of 3.75 cm or greater represents an aneurysm in that person. A variation of this defines an aneurysm when the enlarged aorta is at least twice its normal size.

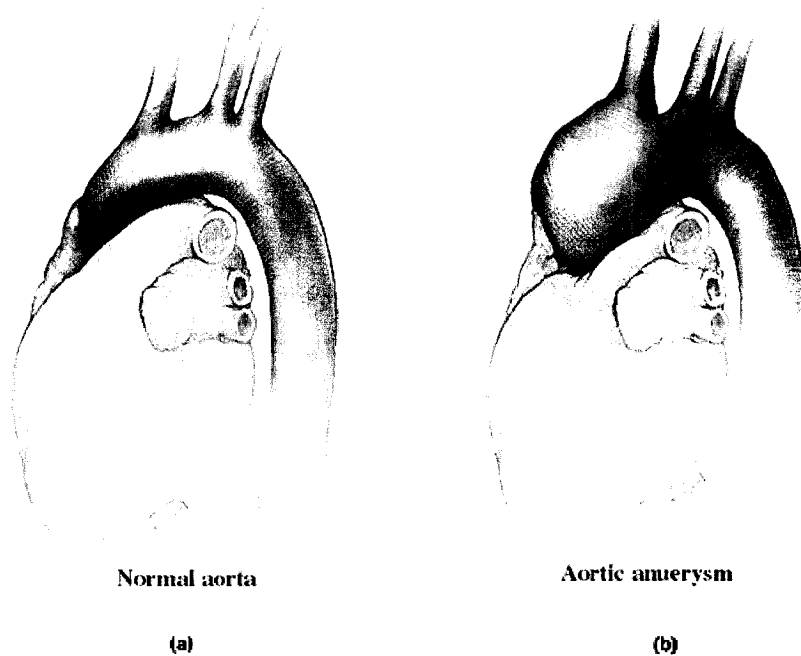


Figure 2.2 (a) Illustration of a healthy aorta – (b) Illustration of an aorta with an aneurysm formed in its ascending part (From Advanced Medical Imaging Laboratory, 2005).

Whether the aorta is called "dilated" or the word "aneurysm" is used, any enlargement of the aorta, regardless of its size, is an indication of aortic disease and requires treatment. Aortic enlargement, although perhaps not yet qualified for the term aneurysm, should be monitored, treated medically, and the lifestyle and diet of the patient addressed as it may lead to annulo-aortic ectasia and aortic regurgitation. Aortic aneurysms are described according to their location, size and shape. Location indicates the sections of the aorta affected (i.e., the root, ascending, arch, descending or thoracoabdominal). The size of the aneurysm is the diameter at the widest point of enlargement and is usually measured in centimeters. In most cases, and if not treated on time, aneurysms lead to wall rupture followed by internal bleeding, rapid loss of arterial pressure, and sudden death.

2.2.3 Aortic Dissection:

The dissection of an artery is the tearing of the inner layer of its wall, allowing blood to leak into the wall itself and cause the separation of the inner and outer layers. Aortic dissection is usually associated with severe chest pain radiating to the back. It may lead to severe blood obstruction or wall rupture. Figure 2.3 describes the details of aortic dissections.

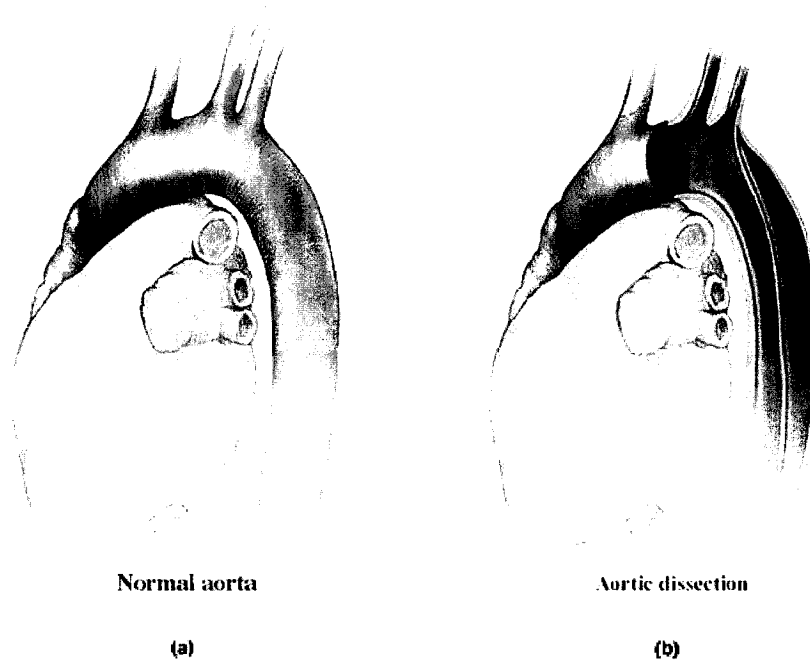


Figure 2.3 (a) Illustration of a healthy aorta – (b) Illustration of an aorta with a dissection formed in its descending part (From Advanced Medical Imaging Laboratory, 2005).

2.2.4 Coarctation of the Aorta:

Coarctation of the aorta is a narrowing of a section of the aorta, typically just beyond the arch as it bends down to descend to the lower body. Blood pressure is lower beyond the narrowed section. This is a congenital condition usually diagnosed and treated in infancy and childhood. It may be present with other congenital conditions such as bicuspid aortic valves.

Coarctation may be present in adults without causing symptoms due to the presence of collateral circulation. This means that over time smaller blood vessels have enlarged and provide an alternative pathway for blood flow. If the mean pressure gradient across the narrowing is greater than 25 mm of mercury, surgery may be needed.

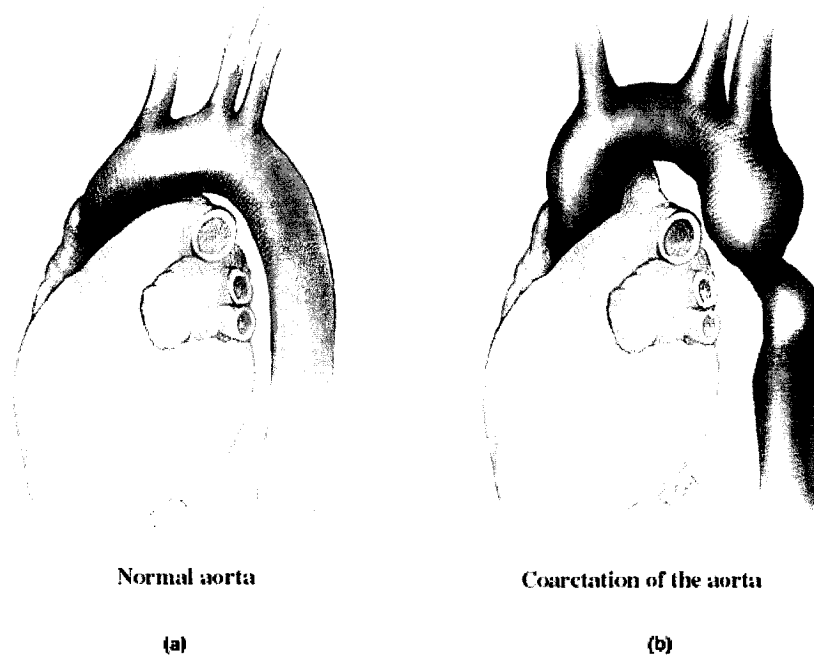


Figure 2.4 (a) Illustration of a healthy aorta – (b) Illustration of an aorta with a coarctation formed in its descending part (From Advanced Medical Imaging Laboratory, 2005).

It is particularly important for adult patients with coarctation to receive treatment for upper body hypertension. Long standing upper body hypertension will cause severe left ventricular thickening (hypertrophy) and increase the risk of stroke as a result of intra-cerebral bleeding. Untreated significant adult coarctation will cause premature death as a result of aortic dissection or hypertension complications.

2.3 Hemodynamics

Numerous investigations point out that there is a relationship between the genesis and the progression of cardiovascular disease with the locally irregular flow occurring in the diseased zone.

Arteries respond to local and global stimuli and adapt to changes in blood flow and blood pressure (Dzau and Gibbons, 1993; Galt et al., 1993). With the progression of vascular disease, the adaptive and healing processes fail and the arteries are often unable to deliver blood in the required amounts and withstand the forces imposed by the blood upon the vessel walls.

Therefore, to examine the relationship between arterial disease and hemodynamic conditions, detailed quantitative data on flow conditions in realistic arterial models is clearly required. In order to study and interpret the flow dynamics in the complex geometry of the human aortic arch, it is important to first understand the effect of simple geometry features on the flow development. As a first step therefore, one should study and understand simple idealized flow models.

2.3.1 Idealized Flow Models

Plug Flow:

The simplest flow one could think of is Uniform Flow: constant velocity of flow in every part of a system. Amazingly, such a simple flow is a fair approximation to actual flow in a simple channel or pipe when the Reynolds number is very low.

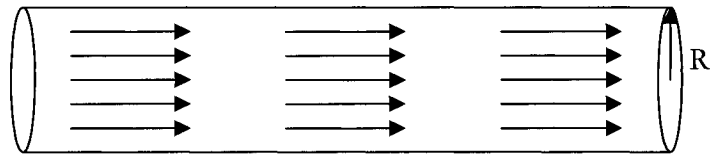


Figure 2.5 Illustration of the velocity profile of a plug flow in a pipe.

Poiseuille Flow:

Lets consider the case of flow in a pipe or channel when Re is very low, however, the flow has been in the pipe for a long distance: The fluid velocity will vary with radial position. This is because the fluid's viscosity will force it to be equal to zero at the walls, and consequently cause the velocity to be small in the vicinity of the walls. Therefore the flow in the center is actually faster for the same volumetric flow.

This flow model was named in the honor of Poiseuille (1799-1869) who performed experiments relating pressure gradient, flow, and tube geometry. In the case of a cylindrical pipe with flow along the axis the velocity distribution is a simple quadratic where:

$$U = 2 \frac{Q}{A} \left[1 - \frac{r^2}{R^2} \right] \quad (2.1)$$

With U the velocity in (m/s), Q the flow rate in (m^3/s), A the cross sectional area in (m^2), r the fluid particle location within the pipe cross section in (m), and finally R the radius of the circular pipe in (m).

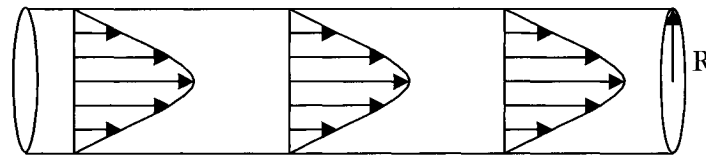


Figure 2.6 Illustration of the velocity profile of Poiseuille flow in a pipe.

The Poiseuille flow model assumes steady flow, however, the flow through the human arteries is pulsatile, consisting of systolic and diastolic phases and the assumption of steady flow is not valid in the major part of the circulatory system and especially in the aorta.

Unsteady Pipe Flow:

Blood flow in arteries is dominated by unsteady flow. In physiological literature, a frequency parameter α , also known as Womersley number is defined to characterize the unsteadiness of flow. The Womersley number is defined by the relationship:

$$\alpha = a\left(\frac{\omega}{\nu}\right)^{0.5} \quad (2.2)$$

Where a is the radius of the tube in (m), ω is the frequency in (s^{-1}), and ν is the kinematic viscosity (m^2/s).

The Womersley number can be interpreted as the ratio of the unsteady forces to the viscous forces (Womersley, 1955). When the Womersley number is low, viscous forces dominate, velocity profiles are parabolic in shape, and the centerline velocity oscillates in phase with the driving pressure gradient. As the Womersley number increases, the unsteady inertial forces start to dominate, and the flow starts to resemble that of a piston-like motion with a plug profile.

Figure 2.7 shows the flow velocity waveform in a normal femoral artery of a dog and the corresponding velocity profiles obtained from the analysis given by Womersley for pulsatile flow in a straight rigid tube. Various velocity profiles are evident through the cardiac cycle. Notice that the velocity profiles are different from the Poiseuille profile; also note that lower velocity near the wall is the first to reverse direction.

This model is limited by the assumption of a fully developed flow in a straight rigid tube and neglects the various area changes and curvatures encountered by blood flow within the human body and therefore is far from physiological flow.

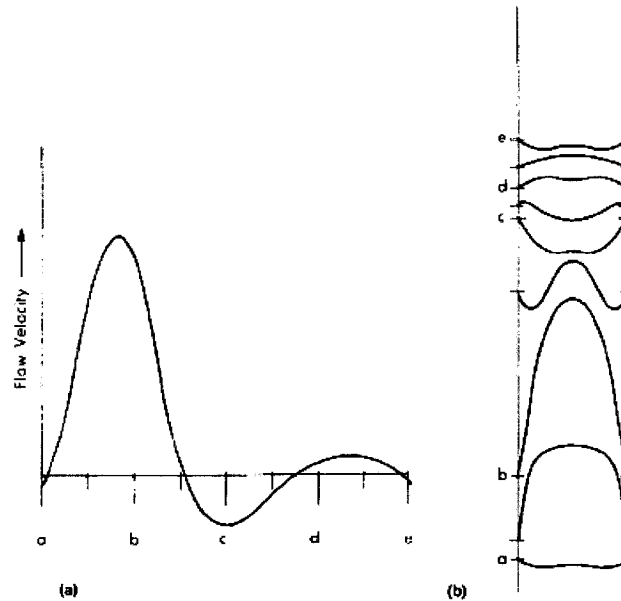


Figure 2.7 (a) Flow velocity waveform in a normal canine femoral arterial flow – (b) Velocity profiles obtained from the analysis given by Womersley for pulsatile flow in a straight rigid tube (Ku, 1997).

Dean's Flow:

In order to study and interpret the flow dynamics in the complex geometry of the human aortic arch, it is important to understand the effect of curvature on the flow development. Dean developed analytical solutions of fully developed, steady flow in a curved tube of circular cross-sections (Dean, 1927). He explained that as the flow moves around the curved tube, an imbalance between the centrifugal forces and the inwardly directed radial pressure gradient results in secondary flow developed within the tube cross section. The fluid in the core moves toward the outer wall of curvature and returns to the inner wall along the tube wall resulting in two symmetric Dean vortices. As the result of the secondary motion, the axial velocity is skewed

with the maximum axial velocity magnitudes found more towards the outer wall with increasing curvature.

The magnitude of the secondary flow and the progressive shift of the maximum axial velocity towards the outer wall is a function of Dean number given by:

$$D = \text{Re} \left(\frac{a}{R} \right)^{0.5} \quad (2.3)$$

Where Re is the Reynolds number, a is the radius of the tube in (m), and R is the radius of curvature of the curved tube in (m).

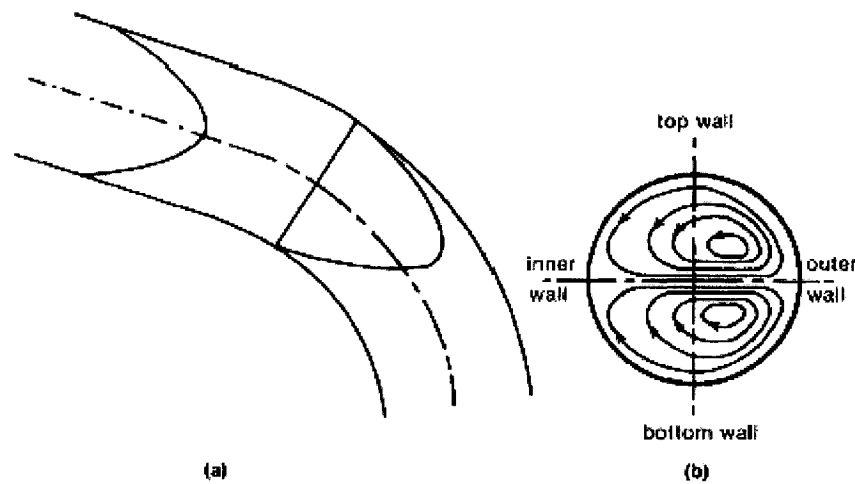


Figure 2.8 (a) Skewing of the axial velocity profile with the maximum velocity toward the outer wall of curvature – (b) In-plane velocity field: the Dean vortices in the cross section (Chandran, 1997).

2.3.2 Cardiovascular Disease and Blood Flow

Numerous investigations point out that there is a relationship between blood hemodynamics (blood fluid mechanics) and localization of atherosclerosis, which can obstruct blood vessels and impede blood flow, and in artery wall degenerative processes that can lead to aneurysm formation and arterial wall dissection (Health Central, 2005).

It has been observed that early atherosclerotic lesions develop preferentially in the vicinity of arterial branching and curvature where blood flow patterns are very

complex and multi-directional (Nerem, 1992; Ku *et al.*, 1985). Wesolowski *et al.* (1965) pointed out that atherosclerosis lesions start in regions of disturbed blood flow, which are in the vicinity of arterial bends and junctions. This had led to the notion that disturbed flow may act as a localizing factor for early atherosclerosis.

Although the biological basis of these observations remains to be determined, flow-induced vascular ECs dysfunction is thought to be involved. Indeed, a large number of *in vitro* studies, including the studies by Resnick *et al.* (1995) and Traub and Berk (1998), have demonstrated that fluid mechanical forces intricately regulate endothelial cell structure and function. In a review article, Davies (1995) explains that mechanical forces associated with blood flow play important roles in the acute control of vascular tone, the regulation of arterial structure and remodeling, and the localization of atherosclerotic lesions. Major regulation of the blood vessel responses occurs by the action of hemodynamic shear stresses on the endothelium.

It has been suggested that atherosclerosis may be initiated at low shear stress locations (Krams, 1997). For instance, and in the case of the coronary arteries, which naturally bend along the surface of the pericardium, atherosclerosis develops more frequently on the inside of the bend, where velocities and shear are lower (Sabbah *et al.*, 1986; Tsutsui *et al.*, 1998). Friedman *et al.* (1981) noted increased intimal thickness in regions of low wall shear stress along the lateral walls of the abdominal aortic bifurcation. Zarins *et al.* (1983) through a combined autopsy and experimental flow study demonstrated that in the carotid artery, atherosclerosis localizes along the outer wall of the carotid sinus where wall shear stress is low. Yamagushi (1999) studied wall shear variations in asymmetrical arterial branching and suggested that atherosclerosis localizes in areas of high shear stress variations.

Moore *et al.* (1994) measured intimal thickness in the distal abdominal aorta in subjects with minimal atherosclerosis disease and noted a positive correlation between shear variation and intimal thickness and a negative correlation between mean shear and intimal thickening.

Low fluid velocity and recirculation zones, which may occur distal to a stenosis and within aneurysms, may provide favorable conditions to prolonged interaction and adhesion of circulating elements onto the endothelium, which are the most important steps for internalization of the particles by the endothelial cells by means

of endocystosis and junctional infiltration (Asakura, 1990). Rodkiewicz (1975) performed an *in vivo* study to simulate atherosclerotic formations using the aortic arch of the rabbit, which is closest in shape to man, and found that atherosclerosis commences and develops at the branches and within the maximum curvature of the aortic arch. All these locations, being geometrically complex, are all associated with complex blood flow patterns.

Studies have showed that differences in arterial geometry do alter blood flow: For instance, Moore et al. (1999) studied blood flow ($Re = 300$, $\alpha = 2.8$) in aorto-iliac bifurcations and found dependence of velocity and shear stress distributions to the main geometrical features which are the bifurcation angle and the parent to child artery area ratio.

Therefore, to examine the relationship between arterial disease and hemodynamic conditions, detailed quantitative data on flow conditions in realistic arterial models is clearly required.

2.3.3 Blood Flow in Simple Anatomical Geometries

Initially, studies have been performed on simple anatomical geometries such as bifurcations and curved tubes.

Relating to blood flow in bifurcations, Taylor *et al.* (1998) performed a numerical study on an abdominal aortic bifurcation. Zhao et al. (2000) studied blood flow in a realistic model of a human carotid arterial bifurcation. They both found blood flow velocity to be higher at the inner wall, also called the site of the apex. On the outer wall side, opposite to the apex, the velocity was found to be pretty low. Small negative velocities were sometimes found, this means that small flow separation zones are created on the opposite side of the wall. Further downstream of the bifurcations, maximum velocity moves slowly towards the center of the vessel. These findings were confirmed by further investigations by Perktold and Rappitsch (1995), Milner *et al.* (1998), Moore *et al.* (1999), and Perktold *et al.* (2001).

Lee and Fung (1970) examined laminar flow through a tube with an axisymmetric constriction: They found regions of reverse flow, these types of regions are often

called “recirculation regions” and may be a significant factor in the deposition process of blood particles discussed earlier.

There have been several experimental and computational studies of both steady and unsteady flow in curved tubes that have aimed to elucidate the flow field within geometries relevant to flow in the aortic arch such as the ones by Hamakiotes and Berger (1988; 1990), Naruse and Tanishita (1996), Komai and Tanishita (1997), and Qiu and Tarbell (2000). These studies have provided great insight into the complexity of flow patterns in curved tube geometries and have demonstrated the resulting skewness in the velocity profiles, towards the outer wall, as well as the structure of the secondary flow patterns within these geometries. Furthermore, these studies have established the dependence of flow in curved tubes on various geometric and flow parameters including the extent of vessel curvature, blood flow rate, and blood flow pulsatility. In order to elucidate blood flow patterns in the aorta, it is therefore essential to use accurate geometrical models and realistic boundary conditions.

2.3.4 Blood Flow in Aortic Models

Recently, there have been a number of *in vivo* and *in vitro* model experimental studies of flow in the human aortic arch as well as in the arch of several animal models. Yearwood and Chandran (1984), and Chandran (1993) ($Re = 1250$ and $\alpha = 19.5$) have demonstrated that the presence of the aortic arch branches has a pronounced effect on the overall flow field.

Redkiewicz (1975) investigated blood flow characteristics ($1000 \leq Re \leq 1500$ and $19.5 \leq \alpha \leq 28.5$) in the aortic arch of a man. A transparent three-dimensional model was used to find the flow patterns within the aortic arch. A visualization technique proved the existence of highly complex flow patterns in the aortic arch and especially within the branches.

In this study, Redkiewicz (1975) showed that as blood is going through the aortic arch, a major portion of flow within the outer wall is diverted into the branches where recirculation zones are created within the proximal distal wall of the branches. The rest of the flow is channeled through the aortic arch and into the descending

aorta. One should also notice the existence of a recirculation zone within the inner wall of the aortic arch.

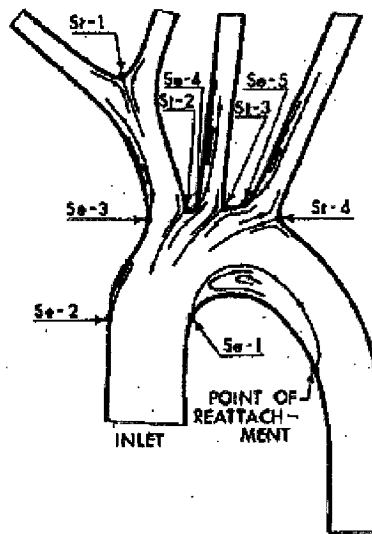


Figure 2.9 Main flow patterns within the aortic arch (Redkiewicz, 1975).

Shahcheraghi *et al.* (2002) performed a fluid flow analysis of a three-dimensional and pulsatile blood flow (Peak $Re = 2500$ and $\alpha = 10$) in a human aortic arch and its three major branches. The geometrical model was derived from the three-dimensional reconstruction of a series of two-dimensional slices obtained *in vivo* using CAT scan imaging of a human aorta. Results demonstrated that the primary flow velocity is skewed towards the inner aortic wall in the ascending aorta. Within the aortic branches, the flow velocities were skewed to the distal walls with flow reversal along the proximal walls. Important secondary flow motion was observed in the aorta, and the structure of these secondary flows was influenced considerably by the presence of the branches. Within the aorta, wall shear stresses were highly dynamic, but were generally high along the outer wall in the vicinity of the branches and low along the inner wall, particularly in the descending aorta. Within the branches, the shear stresses were considerably higher along the distal walls than along the proximal walls. Wall pressure was low along the inner aortic wall and high around the branches and along the outer wall in the ascending aorta. Comparison of the numerical results with

the localization of early atherosclerotic lesions broadly suggests preferential development of these lesions in regions of extrema (either maxima or minima) in wall shear stress and pressure.

However, this study has major limitations: At the aortic inlet, a flat or plug flow velocity profile was used together with a pulsatile waveform based on reported experimental data by Pedley (1980) and justified by *in vivo* measurements by Nerem (1992) using hot film anemometry on various animal models that have demonstrated that the velocity profile distal to the aortic valve are relatively flat. The peak Reynolds number used was 2500 while it is known nowadays that the peak Reynolds number can reach values as high as 7000 according to Stein *et al.* (1976) and Nakamura *et al.* (1993) who measured blood flow velocity in healthy adults using the same hot film anemometry technique.

In addition to the inlet boundary condition, they have imposed additional boundary conditions at the outlet of the aortic branches such that approximately five percent of the flow volume is diverted into each of the three aortic branches as reported by Middleman (1972). The first branch known as the brachiocephalic, however, branches out into two arteries, the right common carotid and the right subclavian which supply respectively the right side of the brain and the right arm and with oxygen rich blood while the left common carotid supplies the left side of the brain and the left subclavian supplied the left arm. Based on these assumptions, the right side of the brain gets half the blood supply of the left side of the brain and similarly, the right arm gets half the blood supply of the left arm which is definitely not physiological.

In fact, and according to Bard (1956), Bell *et al.* (1965), and Guyton (1960; 1971), blood flow is distributed through the aorta such that about seven percent goes into the right subclavian, about four percent into the right common carotid, which means a total of eleven percent into the brachiocephalic artery. Another four percent is approximately diverted into the left common carotid, and about seven percent into the left subclavian. The remaining seventy eight percent goes downstream into the descending aorta.

Chapter 3: Methodology

3.1 Overview

The following chapter presents the methodology taken for the numerical analysis on the hemodynamics of the aorta. The study of hemodynamics in complex shapes such as the aorta requires accurate three-dimensional descriptions of *in vivo* anatomies. Common methods for obtaining such geometries include *in vivo* medical imaging and postmortem preparations such as vessel casts, pressure fixed vessels. Although many studies (Moore *et al.*, 1998; Sun *et al.*, 1994) have shown that the geometry of *in vitro* phantoms can be accurately reconstructed from medical images it was not clear how accurate a reconstruction can be made from *in vivo* clinical images. Moore *et al.* (1999) performed *in vivo* magnetic resonance imaging on aorto-iliac regions of rabbits to study the relative accuracy of all these methods. Results suggest that *in vivo* MRI best replicates overall vessel geometry (vessel geometry and bifurcation angle).

Based on this study, the 3D aorta model used in this study was reconstructed using 2D magnetic resonance imaging MRI data of a healthy adult human aorta. The objective is to use the primary geometrical features of a human aorta to study its hemodynamics.

For this study, cross sectional MRI images of the aorta were obtained from Hospital St. Luc in Montreal: the data consisted of 22 image cross sections with a 1x1x5 mm spatial resolution.

Several processes are required to transform 2D MRI images into a 3D physical numerical model (Fig. 3.1).

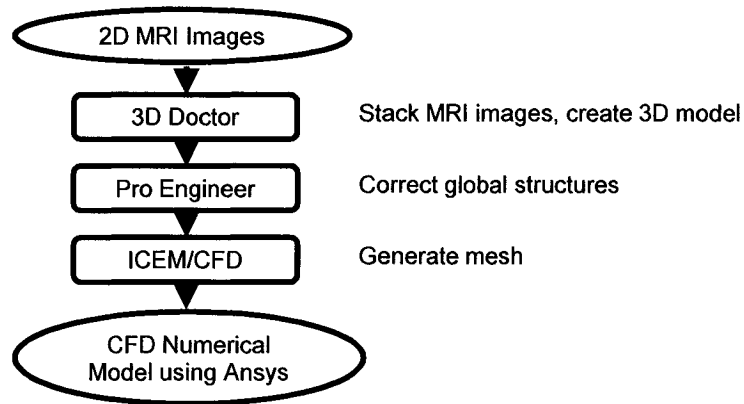


Figure 3.1 Steps required to transform 2D MRI data into a physical numerical model.

3.2 Data Acquisition using Magnetic Resonance Imaging

Magnetic Resonance Imaging (MRI) is a technique used to create images of the body using the principles of nuclear magnetic resonance. Thin sectional images of any part of the body can be generated without surgical intrusion. This can be done from any angle or any direction. The biochemical compositions within the cross sections of any part of the body can be provided by the MRI. Diagnosis of many diseases in their initial stage is often obtained by analyzing these profiles of biochemical compositions.

The series of 2D images in sequence with the correct spacing allows the recreation of its 3D structure. Two different sequences of images were captured: one along the vertical planes, and one along the horizontal planes. These files are stored in DICOM (DCM) format, a standard for medical images.



Figure 3.2 Selected MRI images of the aorta along different vertical planes

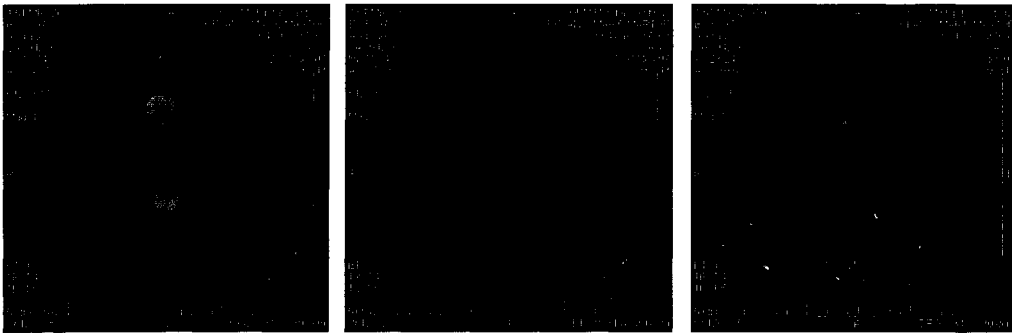


Figure 3.3 Selected MRI images of the aorta along different vertical planes

The 3D reconstruction was performed using 3D-Doctor; an advanced 3D imaging software for 3D imaging applications and US-FDA approved for medical imaging applications.

3.3 3D Reconstruction using 3D Doctor

Created by Able Software Corp., 3D Doctor is an advanced 3D imaging software capable of processing volumetric images from MRI, Computed Tomography (CT), and Positron Emission Tomography (PET) to construct 3D models. Volume measurements, image data handling and other quantitative analysis can be achieved through its editing tools.

The files of the MRI data are not in a standard format which can be read by common CAD software. 3D Doctor is used here to import the DICOM format of the MRI images, render a 3D surface model of the aorta, and then export this model in a format recognizable by other CAD software, such as IGES and VRML. The steps required to accomplish these tasks are provided below:

3.3.1. Image Stack Creation

Once the image slices are selected, they are stored into one file with 3D Doctor as an image “stack”, the DICOM format in this case is useful as the correct order along with the image slices are automatically implemented.

3.3.2. Image Segmentation

Image segmentation defines the boundary of the object at each slice. Auto Segmentation is a convenient tool to detect and trace all object boundaries automatically. However, this option is only viable for images with distinguishable contrast between the object of interest and its surroundings. The provided images of the aorta do not have enough contrast at its boundaries to utilize this option effectively. Interactive Segmentation was used here because the images of the aorta have a uniform intensity level. Using the interactive segmentation, the boundaries were extracted from each image by manually adjusting the threshold levels.

Figure 3.4.a shows an ascending and descending cross section of the aorta, the green lines represent the boundary whereas the red represent the horizontal slice of the lumen. The interactive segmentation dialogue box is shown in figure 3.4.b where the image thresholds values allow a greater control on the final segmentation results.

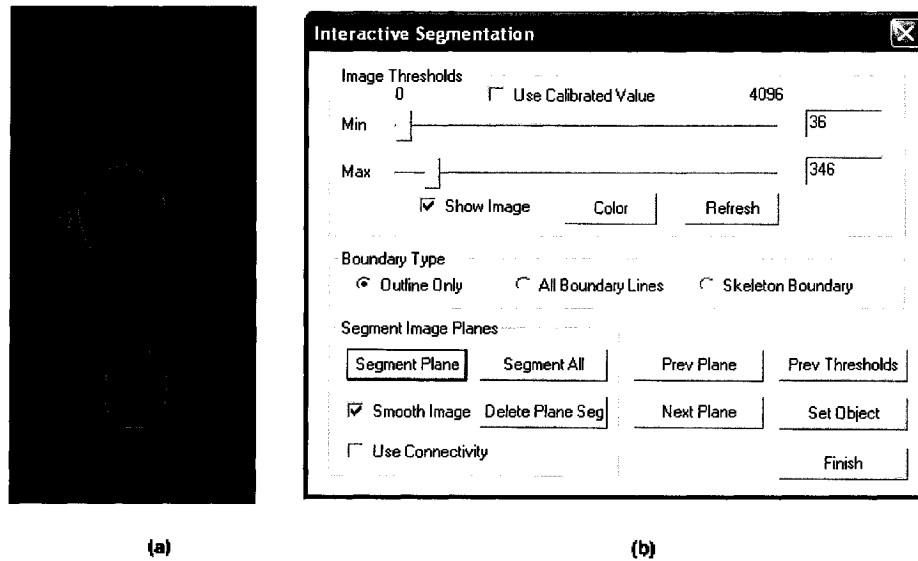


Figure 3.4 (a) Cross section of the aorta being segmented
 – (b) Interactive segmentation dialogue box.

3.3.3. Boundary Editing

Because some areas have the same grey shade as the object of interest, these are sometimes automatically selected and segmented. As can be seen in figure 3.4.a, undesired red pixels are left in some areas. The boundaries created around these pixels need to be deleted manually. Also, depending on that amount of contrast in the image, the accuracy of the desired boundaries may vary. Boundary editing is used to delete unwanted boundaries or to reshape existing boundaries to the contours of the object. New boundaries can also be created. The same process is repeated for each image within the image stack.

3.3.4. 3D Surface Rendering

Once the boundaries of all 22 cross sections are defined, a 3D surface is created by the software. The final surface obtained is shown below:



Figure 3.5 Aorta surface created by 3D Doctor and viewed from three different angles.

Even though the 3D reconstructed surface captures all key features of the aorta, it can be seen from the figure above that the model is not completely anatomically correct: First, the luminal surface is rough and not physiological, second the aortic sinuses are not present below the ascending aorta of the 3D model, and third side branches are not complete. This is due to the inability of the MRI to differentiate overlaid anatomical structures with the same properties.

The model therefore needs corrections to better represent the anatomical features. The 3D surface was therefore exported as a VRML file. This file format is recognizable by Pro Engineer, which was utilized for further model manipulations.

3.4 Global Surface Corrections using Pro Engineer:

Pro Engineer (Pro/E) is a computer-aided design (CAD) software used for design and manufacturing of a wide range of products. The program is *featured based*, meaning that parts and assemblies are created by defining features such as extrusions, slots, and holes. Such features reflect common manufacturing techniques. The *parametric* aspect of the software allows features to be specified by assigning values to attributes like direction of creation, reference planes and dimensions. Along with

these advantageous aspects, Pro/E was used because it is a user-friendly package with interfaces to most mesh generation and numerical simulation packages.

The luminal surface obtained was rough and therefore non-physiological. This is because the available MRI technology available to us had a limited spatial resolution of 1x1x5mm.

Moore *et al.* (1999) found that reconstructed models from MRI data of a carotid artery bifurcation were unacceptably noisy, unless luminal profile smoothing and approximating surface splines was performed.

To avoid computational errors introduced by the luminal surface roughness, smoothing of the surface needed to be performed. To do this, the imported model was sectioned at different planes perpendicular to the flow direction. At each cross section, a spline was generated that followed closely its boundary. The set of splines then act as a frame from which a smooth surface connecting all constructed splines can be created. This 3D surface was reconstructed using an advanced 3D spline surface creation method within Pro/E.

In addition, the three branches (brachiocephalic, left common carotid, and left subclavian) were extended in order to avoid “end effects” within the computational solution.

The final reconstructed, smooth, 3D surface included the ascending aorta, the aortic arch, the three branches, and part of the descending aorta.

Figure 3.6 shows the initial aortic 3D model imported into Pro/E and the final aortic model after the corrections were made.

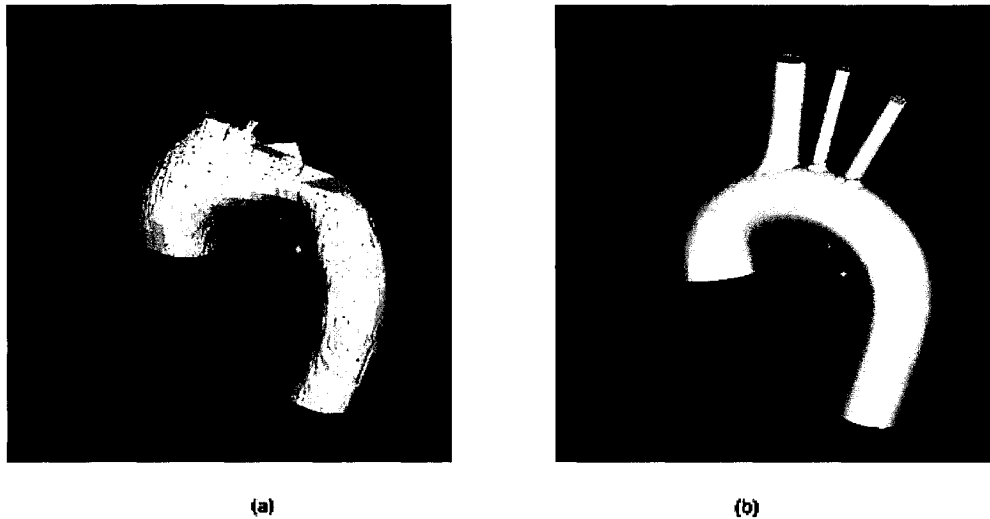


Figure 3.6 (a) Initial aortic model imported into Pro/E – (b) Aortic model obtained after global surface corrections.

3.5 Mesh Generation using ICEM/CFD:

One of the most critical steps in performing 3D simulations is the exportation of the geometry to the meshing software. ICEM/CFD software package was selected because a direct Pro/E interface is available, and because there is an option for mesh optimization with this package. The use of ICEM/CFD eliminates the need to use standard file types in the geometry export process, a step which often leads to lengthy geometric clean-up and other problems.

ICEM/CFD was also used because it takes full advantage of the object oriented unstructured meshing technology. No tedious up-front triangular surface meshing is needed to provide well-balanced start meshes. ICEM/CFD Tetra works directly from the CAD surfaces and fills the volume with tetrahedral elements using the Octree approach where the prescribed curves and points within the geometry to be studied define the positions of the edges and vertices for the mesh generated.

ICEM/CFD Tetra generates the volume mesh and the surface mesh on the object surfaces. This automatic mesh generation tool is suitable to complex geometries and offers tools for local adaptive mesh refinement and coarsening.

Within Pro/E and using the Pro/E-ICEM/CFD interface, family assignments are made and the geometry is exported in ICEM/CFD .tin format.

Meshes were generated by assigning a smaller element size within the branches compared to the element size in the main aorta. A total of six meshes were created with different number of elements based on element size. These meshes were used to make sure that the numerical solution obtained has converged and has reached mesh independence, this will be addressed in more details in the “mesh independence validation” section.

Figure 3.7 shows a mesh of the reconstructed aorta with 120,000 elements. It is difficult to distinguish the elements because the mesh is very dense.



Figure 3.7 Mesh of the reconstructed aorta with 120,000 elements.

3.6 Numerical Analysis using Ansys Flotran

For each mesh, an Ansys input file was created. The Ansys Multi-Physics package was chosen for this study because of its compatibility with the ICEM/CFD software, user-friendliness, powerful Flotran Computation Fluid Dynamics (CFD) solver module, and most importantly because it has already been validated for an exhaustive list of fluid flow problems including flow in circular ducts and bends which are relevant to the geometrical problem in hand.

Flotran solution method uses either 2D or 3D elements for the calculation of 2D and 3D velocity and pressure distributions in a single phase, Newtonian fluid.

The fluid flow problem is defined by the laws of conservation of mass, momentum, and energy. These laws are expressed in terms of partial differential equations which are discretized with a finite element based technique, Ansys (2005).

Assumptions about the fluid and the analysis are as follows:

- There is only one phase.
- The user must determine: (a) if the problem is laminar (default) or turbulent; (b) if the incompressible (default) or the compressible algorithm must be invoked.

For the elements, the velocities and pressure are obtained from the conservation of momentum and the conservation of mass principle. A segregated sequential solver algorithm is used; that is, the matrix system derived from the finite element discretization of the governing equation for each degree of freedom is solved separately. The flow problem is nonlinear and the governing equations are coupled together. The sequential solution of all the governing equations, combined with the update of any temperature- or pressure-dependent properties, constitutes a “global iteration”. The number of global iterations required to achieve a converged solution may vary considerably, depending on the size and stability of the problem.

For numerical accuracy reasons, the algorithm solves for a relative pressure rather than an absolute pressure.

For transient analysis, there are two methods available for the time integration: Backward (the default) and Newmark. The Newmark method is more accurate than the Backward method, Ansys theory manual (2005). In the Newark method, the time

dimension is represented by a set of discrete points each a time increment Δt apart. The system is solved at each of these points in time using as data the solution at a previous time. The value of a function at time $t = n.\Delta t$ with n , an integer. For more information about the Newmark technique, please refer to chapter 17 of the Ansys theory manual (2005), section 2.

For this reason, the Newmark method was used to perform the study. In addition, one must make decisions regarding the time step, the method for the convergence of the analysis during a time step, the length of execution of the job and the frequency of output.

The convergence criteria chosen for the analysis were the following:

- $V_x = 0.0001$ m/s
- $V_y = 0.0001$ m/s
- $V_z = 0.0001$ m/s
- Pressure = 0.0001 Pa.

These criteria were chosen because they represent a good balance between computational cost and accuracy as it won't affect our ability to make conclusions on flow patterns.

For more information about solution algorithms please refer to Ansys theory manual, Ansys (2005).

3.7 Post Processing using Tecplot

For the display of pressure and shear results, Ansys was used as it can be done directly once the solution is obtained without any post processing.

However, for velocity results, and based on previous studies in the aortic arch, we are expecting to get complex flow patterns with important secondary flows. Therefore, it is essential to have the capability to display, both out of plane velocities and in plane velocities, in a same graph to better analyze the results. Ansys post processing module is not sufficient for this task as it can only display one variable with a same graph.

A versatile, user friendly, powerful tool capable of displaying different results on a same graph is needed.

Tecplot 9.2 was chosen because of its extensive 2- and 3-D capabilities for visualizing technical data from analyses, simulations and experiments. Tecplot combines general engineering plotting with high-end 3-D scientific data visualization.

3.8 Governing Equations and Boundary Conditions

3.8.1 Governing Equations

In modeling wall shear stress, the choice of an appropriate constitutive equation for blood is crucial. Determination of an appropriate constitutive model for blood is not trivial: it is a concentrated suspension of blood cells in plasma and exhibits a range of non-Newtonian properties. These properties are mainly governed by the deformation and aggregation of red blood cells. Apart from the fluid properties, flow conditions in large arteries are an important factor in determining an appropriate constitutive equation for blood. In the literature on blood flow in large arteries, blood is generally modeled as a Newtonian fluid, Caro (1978) and Pedley (1980). In addition, the blood is considered to be isothermal and incompressible.

The Newtonian blood is governed by the continuity equation and the Navier-Stokes equation, it can be written as follows:

$$\text{Continuity:} \quad \nabla \cdot \vec{U} = 0 \quad (3.1)$$

$$\text{And Momentum:} \quad \rho \left[\frac{\partial \vec{U}}{\partial t} + (\vec{U} \cdot \nabla) \vec{U} \right] = -\nabla P + \mu \nabla^2 \vec{U} \quad (3.2)$$

Where ρ is the density in (kg/m^3), U the velocity vector (U_x, U_y, U_z) in (m/s), P the pressure in (N/m^2), and μ is the dynamic viscosity in ($\text{Pa}\cdot\text{s}$).

3.8.2 Blood Properties

The density is fixed at $\rho = 1051$ (kg/m^3) and the dynamic viscosity at $\mu = 0.0035$ ($\text{Pa}\cdot\text{s}$) a value based on McDonald (1974).

3.8.3 Boundary Conditions

Doppler flow measurements in arteries have been verified to be reasonably accurate in young individuals, in whom peak systolic velocities represent twice the mean flow (Hatle, 1985), which is equivalent to a fully developed Poiseuille flow. A fully developed Poiseuille flow was therefore used as a boundary condition at the inlet of the ascending aorta.

Figure 3.8 shows the flow waveform used in the numerical analysis. An average flow rate of 5 l/min was used with a peak systolic flow of 20 l/min and a frequency equivalent to an average of 75 beats per minutes. The average Reynolds number used was 1254 and the Womersley number was 19.50, peak Reynolds number within the pulsatile cycle was equal to 5016. These flow rate values were taken from various studies performed by Hatle (1984), Levy *et al.* (1985), Wilson *et al.* (1985), Van Dam *et al.* (1987), and Poutanen *et al.* (2003). In the latest study, by Poutanen *et al.* (2003), normal aortic dimensions and blood flow velocities were measured in 168 healthy children and adults in different locations within the aortic arch including the ascending aorta using digitized two-dimensional and Doppler echocardiography where peak systolic flow reached values equivalent to an instantaneous flow rate of about 20 l/min.

As mentioned earlier, the frequency is equivalent to an average of 75 beats per minute which means that each pulsatile cycle takes place in 0.8 seconds. The flow waveform used is characterized by a systole to diastole ratio of 30/70 unlike the study performed by Shahcheraghi *et al.* (2002) where the systole to diastole ratio is 50/50 which is abnormal for a healthy subject. The flow waveform is also characterized by four events that are of special interest because, based on previous studies, interesting flow characteristics happen during these times within the pulsatile cycle, they are: Maximum flow acceleration taking place 0.06 seconds before the second event, peak systole. 0.06 seconds later minimum acceleration happens followed by peak diastole or flow reversal taking place 0.12 seconds later. Refer to figure 3.8 for more information:

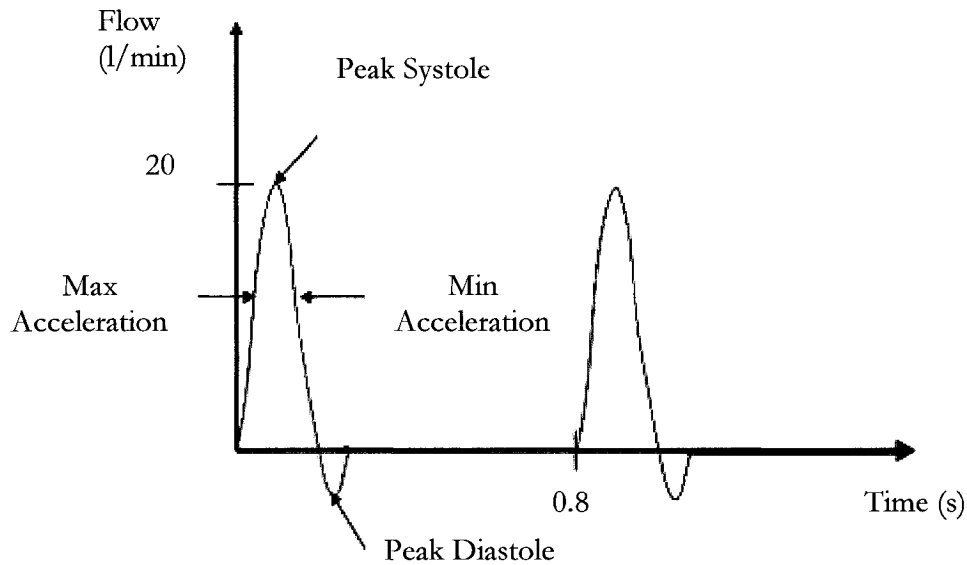


Figure 3.8 Inlet flow waveform used as an inlet flow boundary condition.

3.9 Mesh Independence Validation

Due to the geometric complexity of the aorta model studied, it is very difficult to assess whether or not the mesh generated is suitable for the computational problem at hand. Meshes can be considered unsuitable for various reasons such as the presence of distorted elements but the most common failing of the computational meshes for 3D problems is low spatial resolution and inability to capture local velocity and wall shear stress features.

Mesh independence is therefore key, but insufficient, to validate the computational results and to make sure they are accurate (Freitas, 1993; Roache, 1998).

Typically, one can check the accuracy of the mesh by using one of three approaches: The first approach is to compare computational results with experimental results however it is very difficult to replicate *in vitro* conditions in numerical simulations. In addition, some flow features are very difficult to capture numerically such as symmetry-breaking bifurcations (Fearn *et al.*, 1990). Experimental measurements can suffer from errors such as model misalignment, incorrect positioning of the

measurement system, along with reading and measurement errors (Ethier *et al.*, 2000).

The second approach is to use a very fine mesh but with the lack of comparative results, it is very difficult to assess the accuracy of such large meshes. Taylor *et al.* (1998) used a mesh with 51568 elements to compute the Womersley solution for the fully developed pulsatile flow in a rigid, long, straight tube and found that the finite element solution did not resolve the theoretical velocity profile along the centerline of the vessel during the second half of the cardiac cycle.

A third approach is to use a series of meshes, going from a coarse to a fine mesh, to demonstrate mesh independence. This method is time-consuming and computationally expensive and consequently rarely reported in the computational hemodynamics literature.

Prakash and Ethier (2001) studied mesh independence of an anatomically realistic right coronary artery: Looking at mesh resolution needed to resolve major flow features such as separation zones and wall shear stress features, they found that mesh-independent velocity fields were not very difficult to get whereas wall shear stress fields were much more difficult to obtain. This is expected because an accurate velocity field does not always imply an accurate wall shear stress field since the latter is a lower order computed quantity.

Even though the mesh independence approach is time consuming and computationally expensive, we decided to use it to assess the mesh resolution needed to obtain accurate results. Since mesh-independent wall shear stresses are more difficult to obtain, they were used for validation in meshes with 51865, 73889, 86451, 101269, 109338, and 118338 elements. The model used involved a steady simulation of the aorta model with a fully developed inlet boundary condition.

The mesh characteristics are summarized in table 3.1 below:

Mesh Number	1	2	3	4	5	6
Number of Elements	51,865	73,889	86,451	101,253	109,338	118,338

Table 3.1 Mesh number versus number of elements used.

Six locations were chosen for mesh validation, each location is either upstream or downstream of one the aortic branches. These locations were specifically chosen because we expect to have very complex flow features and shear stress distributions in their vicinity. These locations therefore represent areas where shear convergence will be the hardest to achieve. Figure 3.9 shows the six locations chosen for the mesh validation.

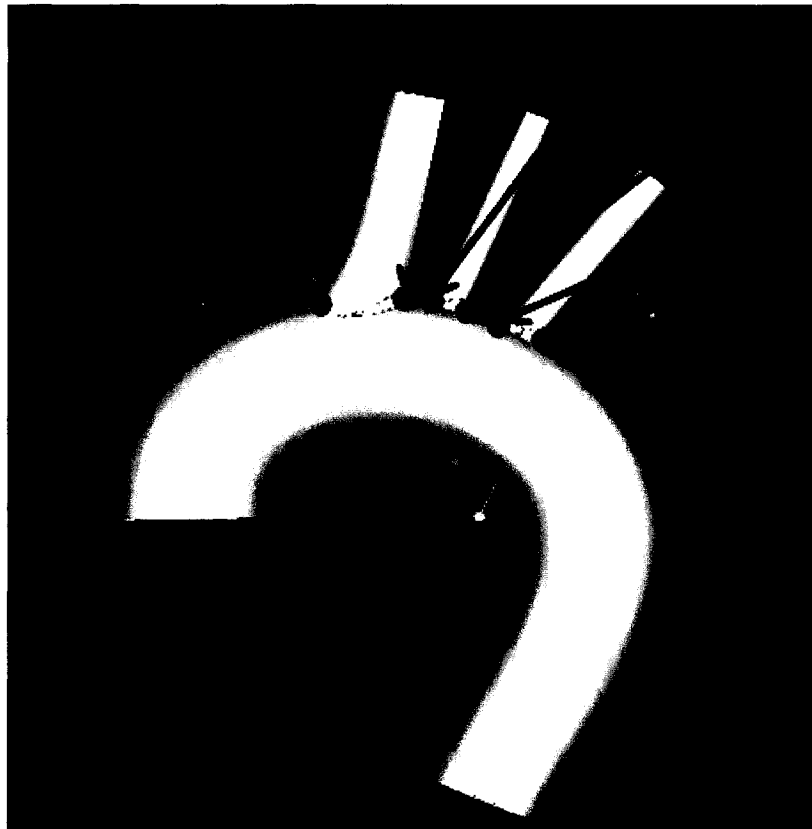


Figure 3.9 Shear locations used for mesh independence validation.

Table 3.2 shows the shear values of the six locations in each of the six meshes studied.

Mesh Number	Wall Shear Stress Values at Selected Locations in Pa					
	1	2	3	4	5	6
1	4.368	1.7918	3.0197	2.6566	2.8563	2.2328
2	3.1793	3.4098	3.5329	4.5462	3.8166	2.9319
3	4.12	4.6173	4.5002	3.6044	3.6315	3.0717
4	5.5707	4.6862	4.1994	4.2154	3.2955	3.282
5	5.1952	4.8941	4.0767	4.0408	4.6809	3.8534
6	4.9938	5.1701	3.9743	3.8419	4.5584	3.6439
% variations between shear values in meshes 5 and 6	3.8	5.7	2.7	5.0	2.6	5.5

Table 3.2 Shear values in the different locations for the different meshes and percentage difference between values obtained in the last two meshes.

For better visualization, the values are plotted on figure 3.10. As can be seen in figure 3.10, wall shear stress distributions show some mesh independence with the later two models showing similar trends and similar magnitudes.

Throughout the model, the wall shear stress results differ only slightly within the last two densest meshes with an average change, within the same location, equal or less than 6%. In fact, one can notice that in figure 3.10, the line representing the values of mesh number 5 almost coincides with the line representing the values for mesh number 6. The mesh can therefore be considered significantly resolved.

Shear stress of the different meshes at selected locations

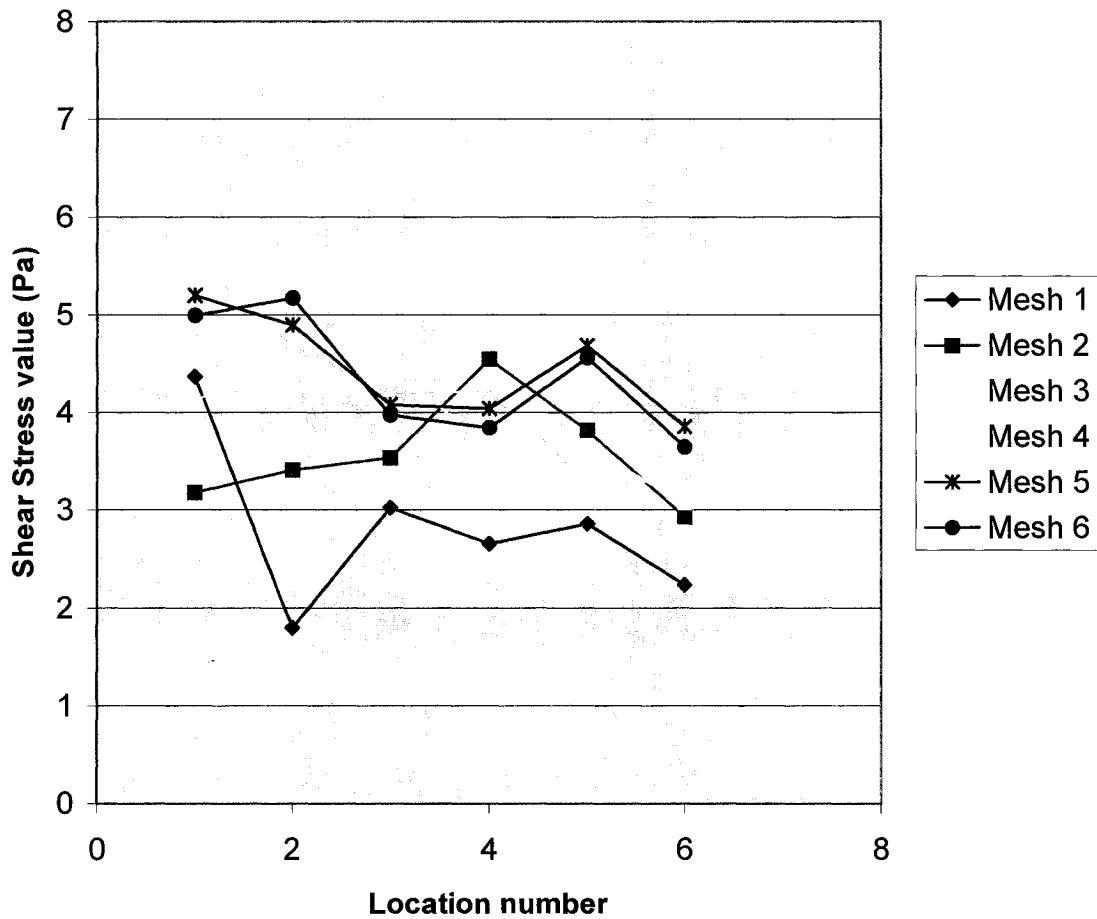


Figure 3.10 Shear values in the different locations for the different meshes.

The errors in wall shear stress are expected to be slightly higher for unsteady flow simulations, since unsteady effects tend to localize in the near wall region but considering all factors, it was decided that a mesh size of 101,253 elements represents an acceptable balance between computational cost and model accuracy for the goals of this study. This mesh and the equivalent mesh resolution were therefore used for all subsequent runs.

Chapter 4: Flow Hemodynamics in the Aortic Arch

4.1 Flow Distribution into the branches

As discussed earlier, Bard (1956), Guyton (1960), and Bell *et al.* (1965), found that blood is distributed in such a way that approximately 11 percent is diverted through the brachiocephalic, 4 percent is diverted to the left common carotid, about 7 percent to the left subclavian, and the rest to the descending aorta which is about 78 percent.

Shahcheraghi *et al.* (2002) imposed boundary conditions at the outlet of the aortic branches such that five percent of the flow volume is diverted into each of the three aortic branches far from the above measured values.

In this thesis, flow in the branches was not imposed so we went back and looked at the flow distributions into the branches to assess how close we are to the physiological values. Flow rates for each time step within the pulsatile cycle were compiled for the inlet and for the four exit boundaries (brachiocephalic, left common carotid, left subclavian, and descending aorta) and were summed. The total for each exit boundary was divided by the total inflow to get the flow distribution ratio. Table 4.1 shows the value for each exit boundary.

Flow distribution within the aorta (%)				
Results	Descending	Brachiocephalic	LCC	LSC
Numerical	77.42	13.59	3.29	5.50
Bell <i>et al.</i> (1965)	78.00	11.00	4.00	7.00
% Variation	0.74	23.54	17.75	21.43

Table 4.1 Flow distribution within the aorta.

As it can be seen, the results agree better with Bell *et al.* (1965) compared to the Shahcheraghi *et al.* (2002) where percentage variations were between 25% (for the LCC) and 120% (for the brachiocephalic). This is the major contribution of the study

as we were able to get numerical results that were closer to the measured physiological values.

4.2 Flow Velocity Results

4.2.1 Overview

The flow results of six different locations will be presented for a pulsatile flow with an average Reynolds number of 1254 and a Womersley number of 19.50.

Six axial cuts or slices within the aortic model, three within the main aorta where one is taken within the ascending aorta, one within the aortic arch between the brachiocephalic artery and the left common carotid, and the third slice within the descending aorta, were extracted from the simulations for detailed presentation. The three others are respectively within the brachiocephalic artery, the left common carotid, and the left subclavian artery.

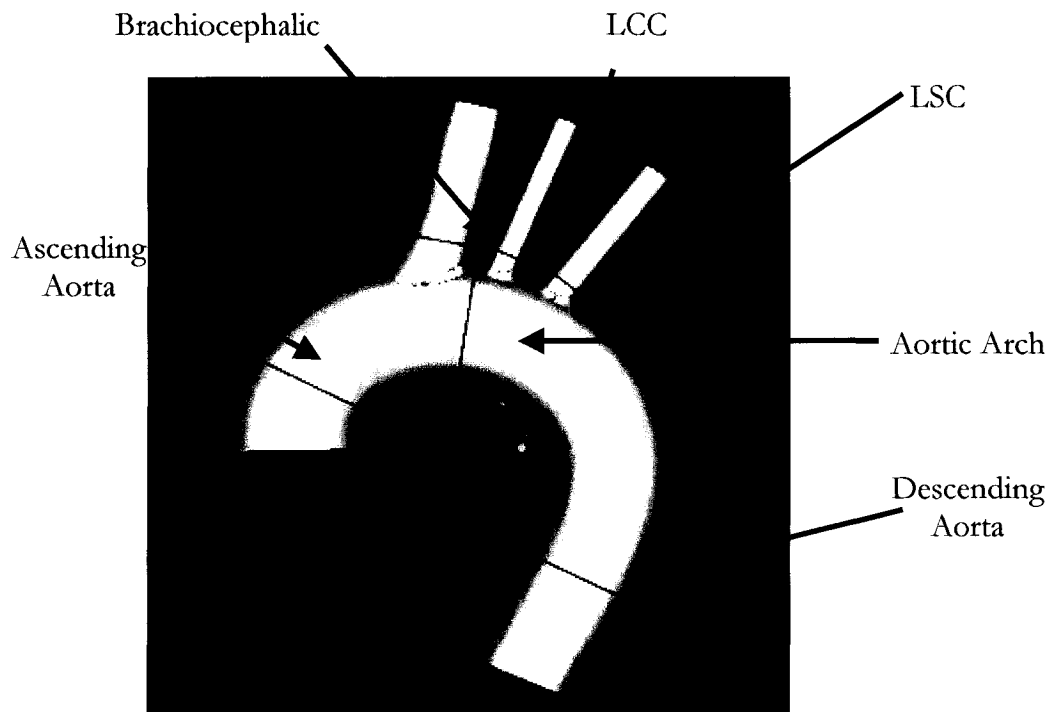


Figure 4.1 Slice locations used for velocity distribution result display.

Figure 4.2 shows the axial velocity within the central plane of the aorta at peak systole. One can notice that because of the complexity of the model, the velocity is highly skewed and changes in distribution from one location to the other.

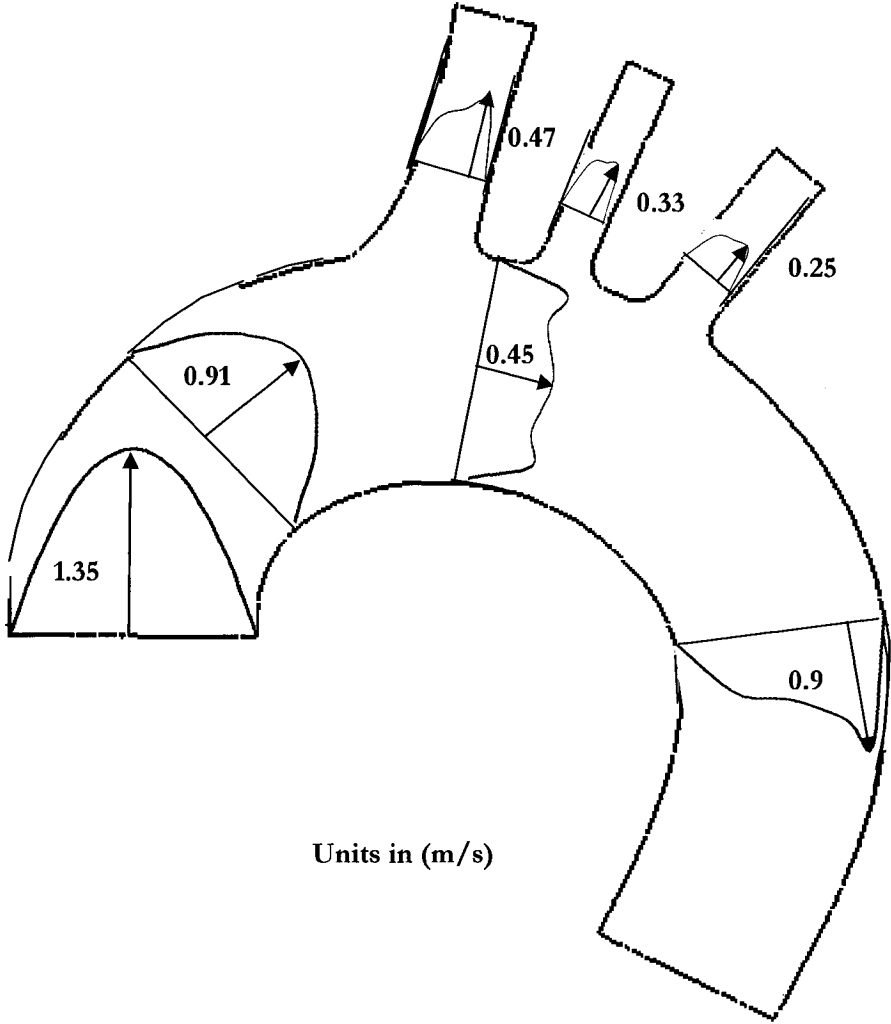


Figure 4.2 Axial Velocities at the selected cross sections within the central plane of the aorta at peak systole. The units are in m/s.

For detailed analysis, and to be able to get information about a larger portion of the flow, we will display the results in a fashion similar to Shahcheraghi *et al.* (2002) study: The results of four different times within the pulsatile cycle will be displayed; they correspond to the four events discussed earlier in section 3.8.3 which are at peak maximum flow acceleration, peak systolic flow, maximum flow deceleration, and peak flow reversal. These four time points were chosen because they represent moments where flow physics are most complex.

4.2.2 Velocity Results

Ascending Aorta:

Figure 4.3 shows the velocity distribution within the ascending aorta at maximum flow acceleration, peak systole, maximum flow deceleration, and peak diastole.

The color contour plot shows the primary or out of plane velocities and the vector plot shows the secondary or in plane velocities. Note that the results are displayed such that the view point is from a distal position with the outer wall positioned at the left and the inner wall at the right.

During peak flow and maximum flow deceleration, the high momentum fluid is located within the central portion and is slightly skewed to the outer wall. During maximum acceleration a blunter profile is seen as in the case of peak reversal. As discussed by McDonald (1974) and Caro (1978), retrograde flow in the aorta at this point of the cycle likely provides blood flow to the coronary arteries. Strong secondary flow, from the outer to the inner wall, is also induced by the curvature as in a simple curved pipe flow. It is interesting to note that during maximum deceleration and peak diastole, secondary flow form complex patterns where flow direction is reversed going from the outer wall into the inner wall and going from the arterial wall into the lumen. These interesting flow patterns have also been reported by Shahcheraghi *et al.* (2002) and are explained by the combined effects of the curvature and the area constriction of the main arch as it resembles a tapered curved tube.

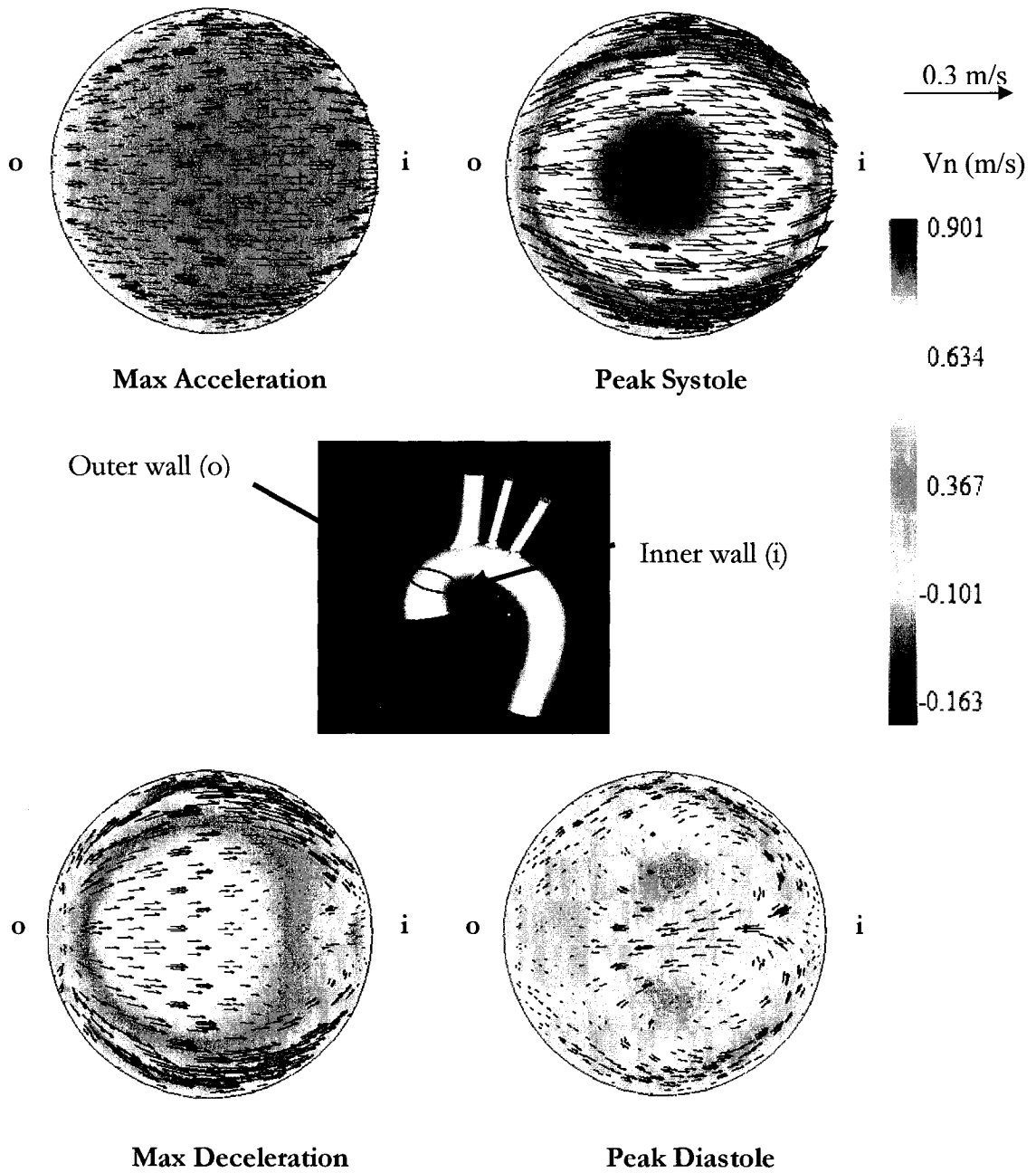


Figure 4.3 Velocity distributions within the ascending aorta at the four time points of interest. The central figure shows the location of the cross section area within the model. Looking at the cross section, the outer wall of the aorta is located at the left and the inner wall at the right.

Aortic Arch:

Figure 4.4 shows the velocity distribution within the aortic arch, distal to the brachiocephalic and proximal to the left common carotid, at four points within the pulsatile cycle: At maximum flow acceleration, peak systole, maximum flow deceleration, and peak diastole.

Similar to the previous plots, the color contour plot shows the out of plane velocities and the vector plot shows the secondary flow velocities. The results are displayed such that the view point is from a distal position with the outer wall positioned at the top and the inner wall at the bottom.

In peak systole, one can notice that the high momentum flow is skewed towards the lateral sides of the aortic arch walls, this is because part of the high momentum flow that occurs within the outer wall was diverted into the brachiocephalic and to the fact that the high momentum flow within the lateral sides did not have time to be diverted into the brachiocephalic but instead went downstream. The flow then loses momentum during flow deceleration and reverses mainly within the outer wall of the aortic arch. This flow reversal is mainly due to branches' blood discharge back into the aortic arch during this phase.

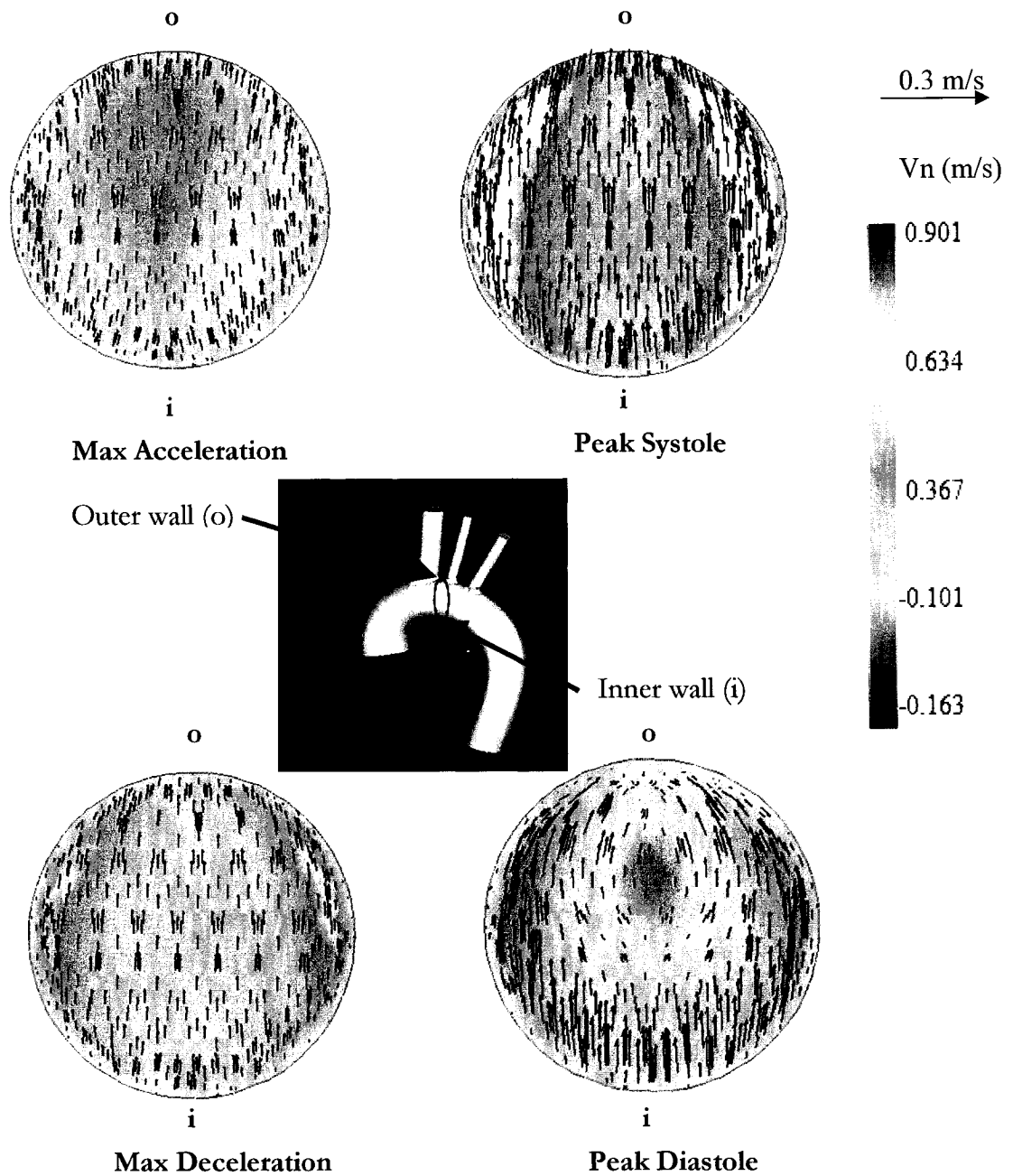


Figure 4.4 Velocity distributions within the aortic arch at the four time points of interest. The central figure shows the location of the cross section area within the model. Looking at the cross section, the outer wall of the aorta is located at the top and the inner wall in the bottom.

Descending Aorta:

Figure 4.5 show the velocity distribution for the descending aorta at maximum flow acceleration, peak systole, maximum flow deceleration, and peak diastole within the descending aorta. For these figures, and to keep the same positioning of the outer and inner wall, i.e. the outer wall at the left and the inner wall at the right, the viewing point is from an upstream position within the aorta.

The high momentum flow is skewed towards the outer wall as in the case of flow in curved tubes. During the majority of the pulse cycle, the higher pressure of the outer wall returns some of the high momentum fluid to the inner wall. Secondary flows within the descending aorta form patterns that are similar to the ones observed in the ascending aorta. However, and compared to secondary flow in the ascending aorta, the magnitudes in the descending aorta are significantly lower.

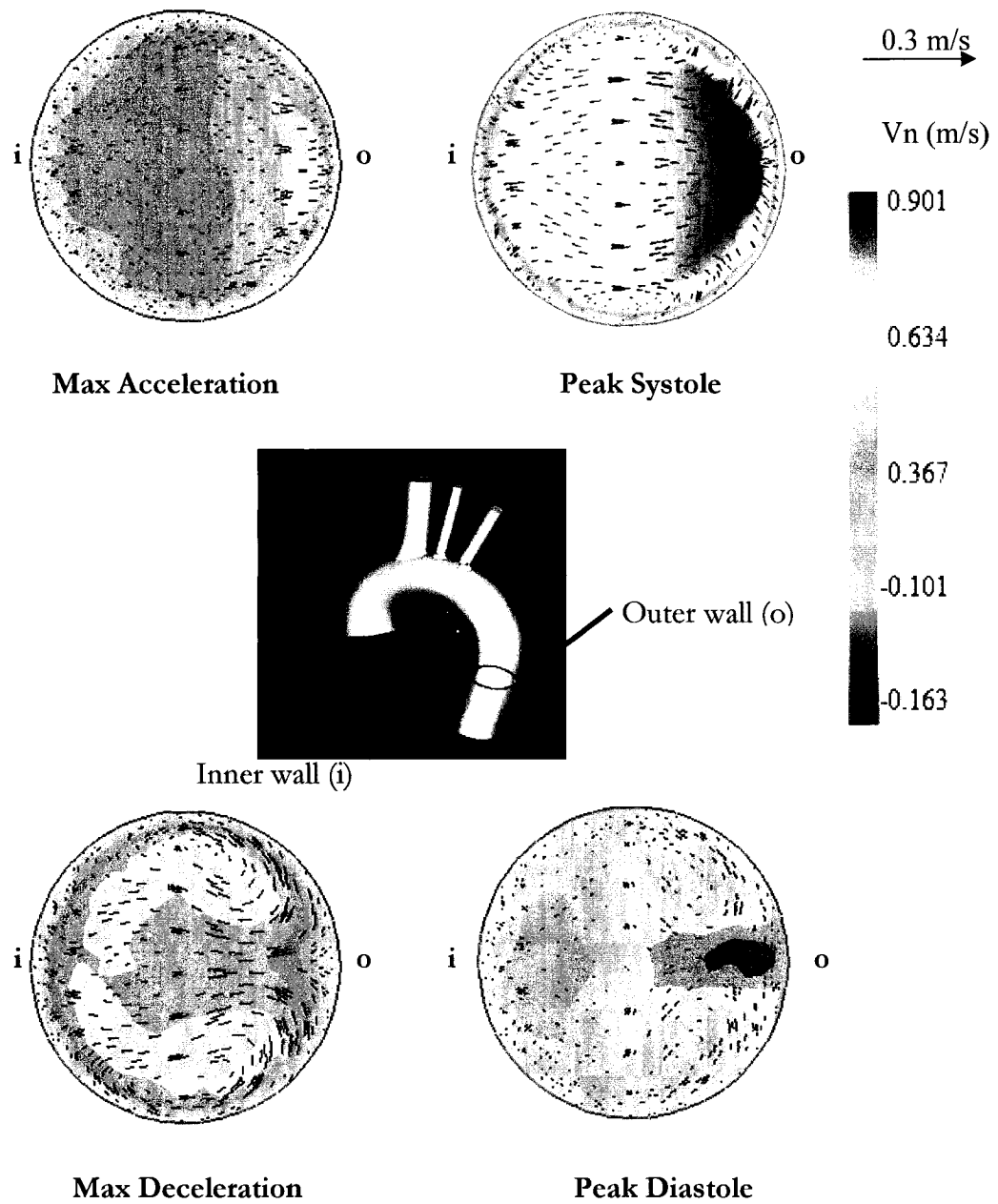


Figure 4.5 Velocity distributions within the descending aorta at the four time points of interest. The central figure shows the location of the cross section area within the model. Looking at the cross section, the outer wall of the aorta is located at the right and the inner wall at the left.

Brachiocephalic Artery:

Figure 4.6 shows the blood flow velocity distribution within the brachiocephalic artery respectively at maximum flow acceleration, peak systole, maximum deceleration, and peak reversal. The figures are laid out such that the distal wall is at the right while the proximal wall is at the left.

Primary flow is highly skewed towards the distal wall of the artery especially in peak systole where high momentum flow forms a pattern similar to a horseshoe facing the distal wall. As blood is gaining momentum throughout the systolic phase, secondary flows is mainly directed from the proximal wall to the distal wall, there is however an additional secondary flow developing from the proximal arterial wall towards the distal central section which is due to the abrupt area constriction going from the main arch into the brachiocephalic artery.

During maximum deceleration, primary flow is reversed at the proximal wall and secondary flow forms patterns similar to the one observed in the ascending aorta cross section. Fluid near the arterial wall is directed into the lumen. It is interesting to note that secondary flow in the brachiocephalic is lower in magnitude compared to secondary flow in the main arch. However, the values are quite significant compared to the primary flow values.

During peak diastole, primary flow is reversed with a nearly axisymmetric profile. Secondary flow, also reversed, is mainly directed from the distal wall towards the proximal wall.

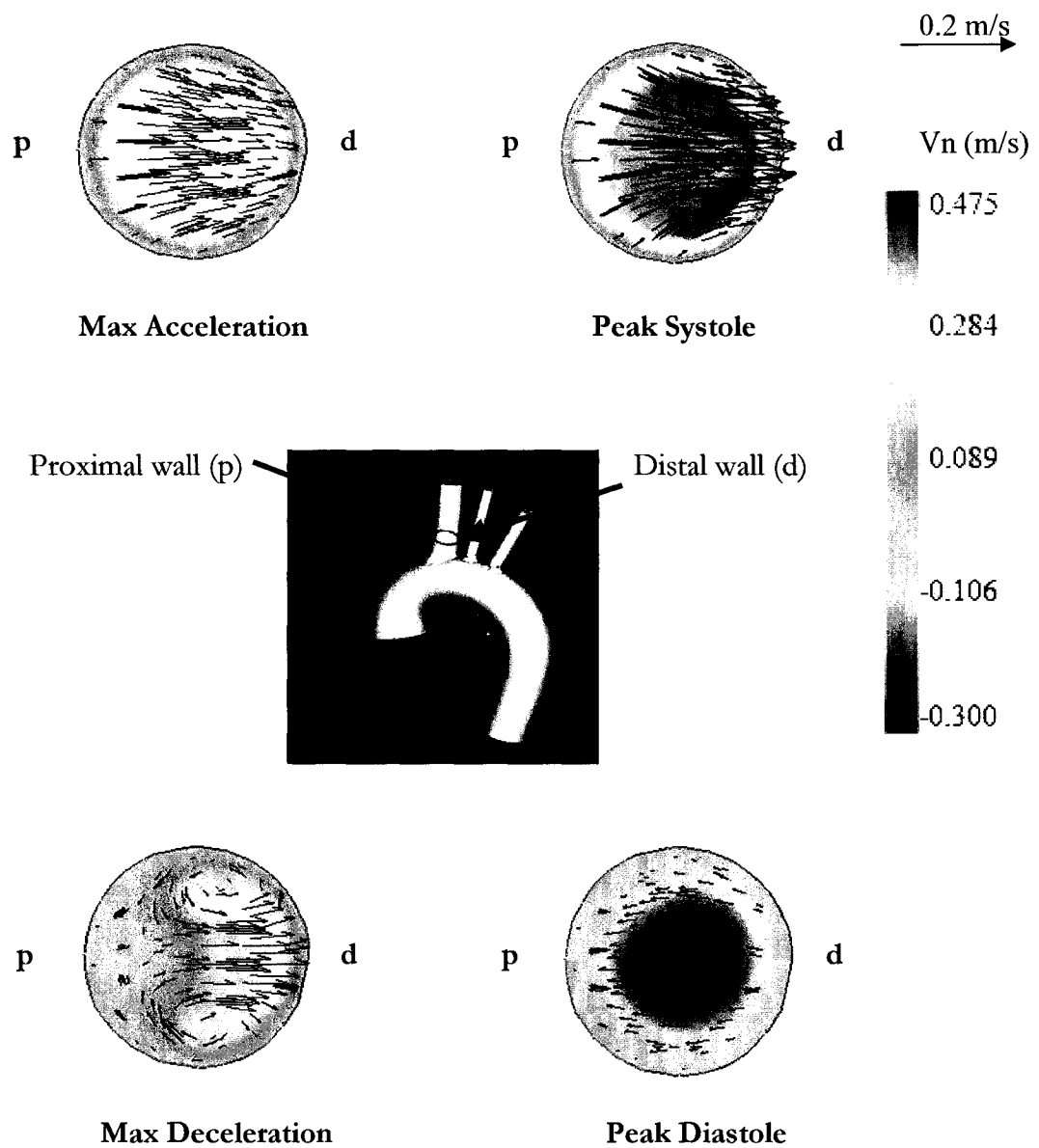


Figure 4.6 Velocity distributions within the brachiocephalic at the four time points of interest. The central figure shows the location of the cross section area within the model. Looking at the cross section, the distal wall of the branch is located at the right and the proximal wall at the left.

Left Common Carotid:

Figure 4.7 shows the flow velocity distribution within the left common carotid at maximum acceleration, peak systole, maximum deceleration, and peak diastole. The figures are oriented in the same fashion where the distal wall is at the right and the proximal wall at the left. Primary flow is skewed towards the distal wall of the artery especially in peak systole where high momentum flow forms a pattern similar to a horseshoe facing the distal wall; it is however not skewed to the levels observed in the brachiocephalic. As blood gains momentum throughout the systolic phase, secondary flows are mainly directed from the proximal wall to the distal wall. Flow patterns during maximum deceleration and peak reversal are also similar.

It is interesting to note that flow magnitudes, however, are lower compared to the magnitudes within the brachiocephalic artery. This is because lower momentum flow passing distal to the brachiocephalic is diverted to the left common carotid as the high momentum flow within the outer wall proximal to the branches was first diverted to the brachiocephalic.

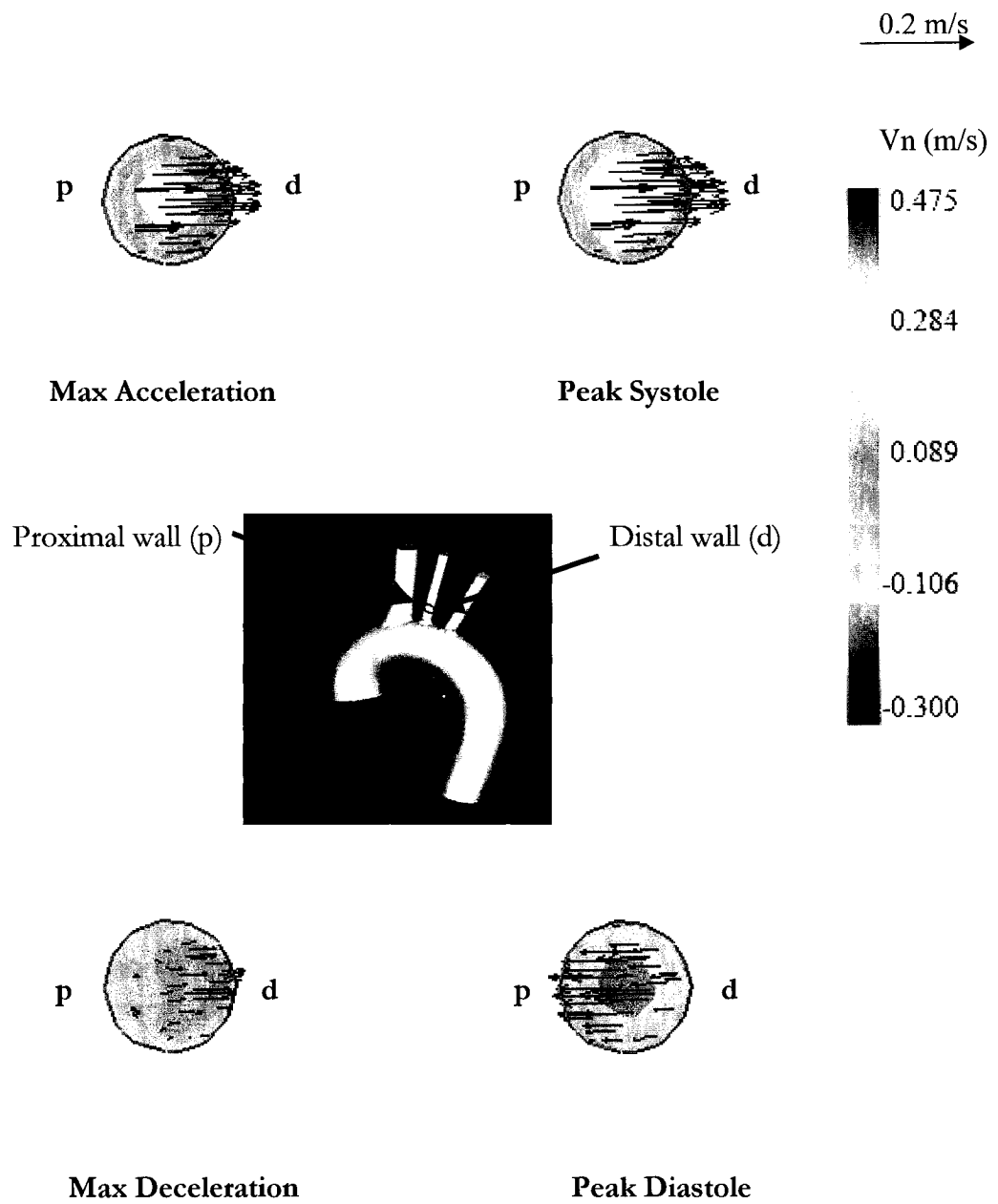


Figure 4.7 Velocity distributions within the left common carotid at the four time points of interest. The central figure shows the location of the cross section area within the model. Looking at the cross section, the distal wall of the branch is located at the right and the proximal wall at the left.

Left Subclavian Artery:

Figure 4.8 shows the flow velocity distribution within the left Subclavian artery at maximum acceleration, peak systole, maximum deceleration, and peak diastole. Primary flow is slightly skewed towards the distal wall of the artery. As blood gains momentum throughout the systolic phase, secondary flows are mainly directed from the proximal wall to the distal wall. Flow patterns during maximum deceleration and peak reversal are also similar to the ones observed in the left common carotid artery. Similarly, flow magnitudes are lower compared to the magnitudes within the left common carotid. This is because lower momentum flow passing distal to the left common carotid is diverted to the left subclavian as the high momentum flow within the outer wall proximal to the branches was first diverted to the brachiocephalic and then to the common left carotid.

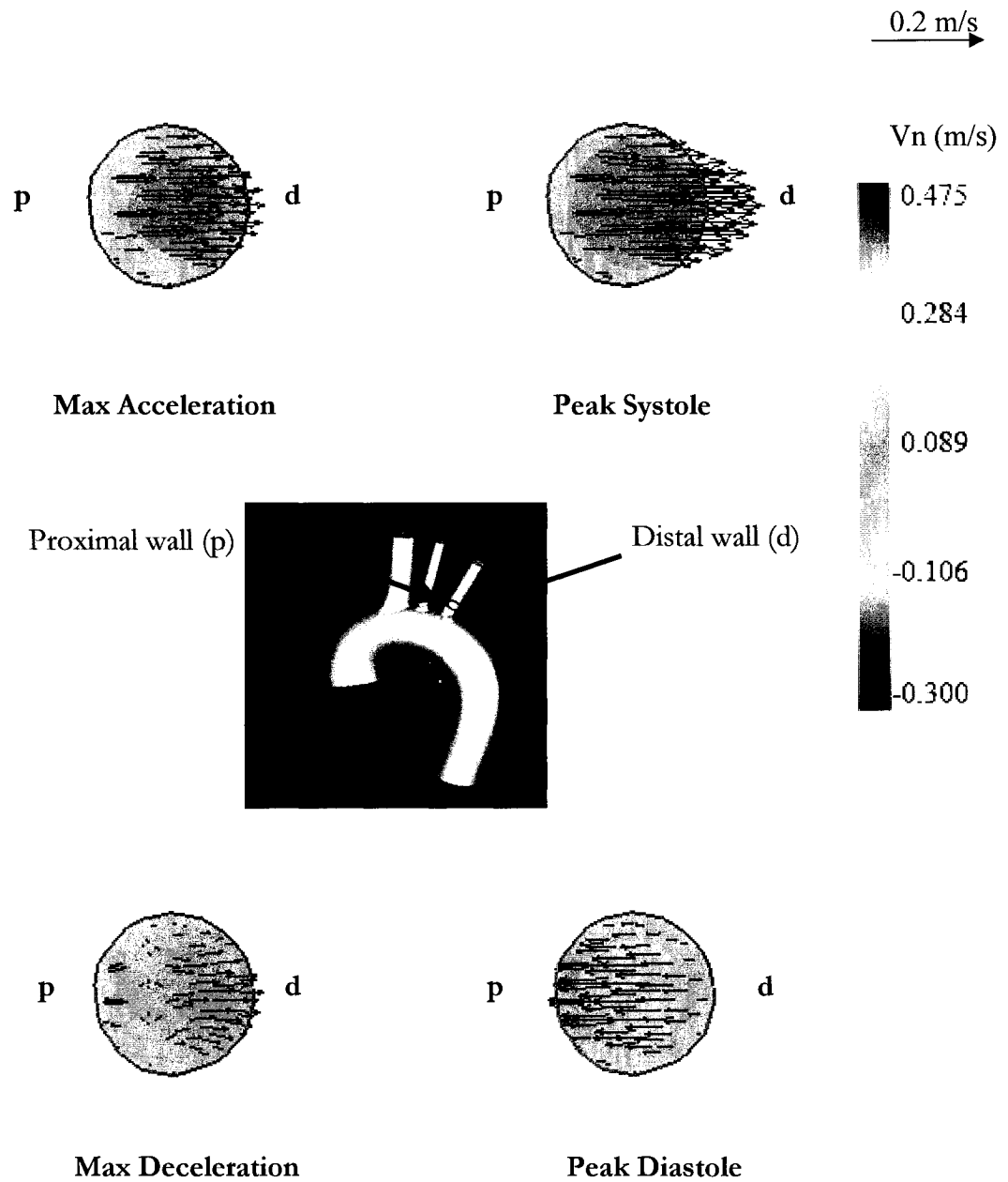


Figure 4.8 Velocity distributions within the left subclavian at the four time points of interest. The central figure shows the location of the cross section area within the model. Looking at the cross section, the distal wall of the branch is located at the right and the proximal wall at the left.

4.3 Pressure Results

The wall pressure contours are presented in figure 4.9. The pressure values were converted from the output units in Pascal into millimeter of mercury (mmHg) for ease of interpretation. As the flow picks up momentum, overall pressure values increase within the aorta and decreases with flow reversal and during diastole.

It is interesting to note that during maximum acceleration and during peak systole, pressure is maximum at the three stagnation regions that are distal to the three branches within the aortic arch. In these regions, the high velocity flow from the aorta is suddenly diverted into the branches which explains the rapid pressure decrease downstream the branches.

Another high pressure region is the outer wall within the ascending aorta, where the sharp curvature decelerates the high momentum flow.

Low pressure regions are located within the proximal walls of the branches at the junction within the outer wall of the aorta. Overall, the lowest pressure values are observed downstream of the branches, within the downstream portion of the inner wall of the aortic arch, and in a large portion further downstream within the descending aorta.

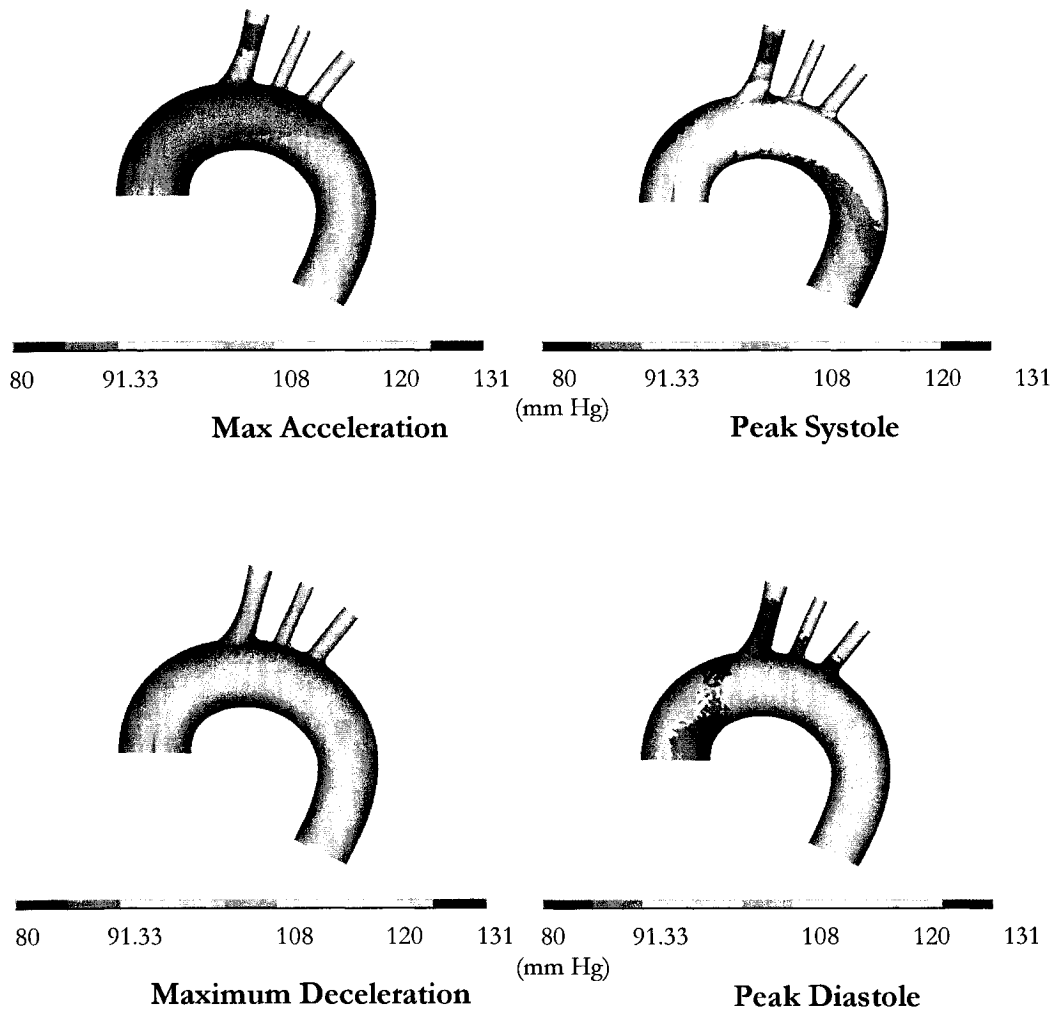


Figure 4.9 Pressure distributions within the central plane at the four time points of interest. The units are in mmHg. 1 mmHg is equal to 133.3 Pa.

4.4 Shear Results

With respect to blood hemodynamics involvement in the development of cardiovascular disease and particularly atherosclerosis, wall shear is probably the most important parameter.

Figure 4.10 shows wall shear rate distribution within the aortic model. The values of wall shear rate presented below are the shear rate magnitudes due to all three components of the velocity vector and the unit is s^{-1} . Overall shear rate increases as the flow picks up momentum from maximum acceleration into the peak systolic phase. At peak systole, wall shear rate maximum occurs on the outer wall of the aorta proximal to the first branch, the brachiocephalic. This probably occurs because the lower pressure in the brachiocephalic artery creates a suction effect. One can also notice that other wall shear rate maxima occur on the outer wall between the branch entrance locations and within the branches. The minimum shear stress areas occur within the inner wall of the aorta especially downstream, in the branches along the proximal walls, and in the descending part of the aorta.

As the flow decelerates overall shear rate values decrease and then increase back again during peak flow reversal especially in the outer wall of the aorta along the branches.

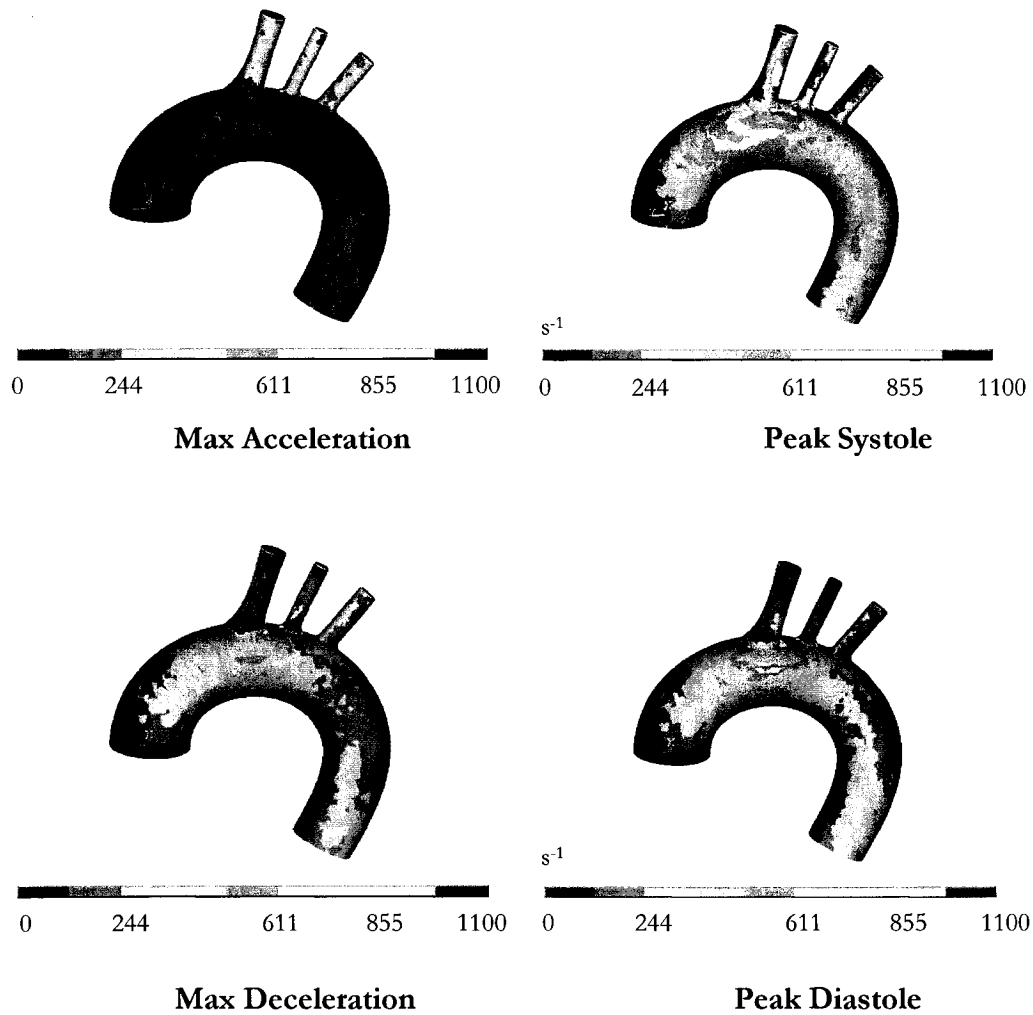


Figure 4.11 Shear rate distributions within the aortic wall at the four time points of interest. The units are in (s^{-1}).

These findings motivated an investigation of the local shear rate time history at specific locations within the aortic model. Six points were chosen for the investigation: As shown in figure 4.11, point 1 is taken within the outer wall of the ascending aorta, point 2 is taken within the outer wall of the aortic arch proximal to the brachiocephalic artery, point 3 is taken within the outer wall of the aortic arch distal to the brachiocephalic and proximal to the left common carotid artery, point 4 is taken distal to the left common carotid but proximal to the left subclavian artery,

point 5 is taken still within the outer wall of the aortic arch distal to the left subclavian. Finally, point 6 is taken within the inner wall of the aortic arch and located in its middle section.

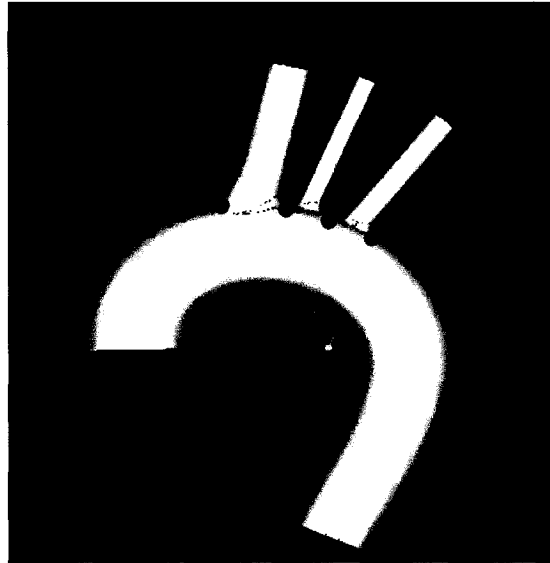


Figure 4.11 Locations for shear rate time history investigation.

Figure 4.12 shows the time history of the wall shear rate magnitude for the six locations during the entire pulsatile cycle. The first thing that one can notice is that the wall shear rate magnitude throughout the pulsatile cycle follows up a pattern that resembles the inlet velocity waveform. As the flow is accelerating, shear rate values increase to reach maximum values. As the flow is decelerating within the end of the systolic phase, shear rate values decrease and stay at relatively low levels throughout the diastolic phase. Point 1, which is located within the outer wall of the ascending aorta, is a fine example. As you can see from figure 4.12, its shear rate history closely resembles that of the inlet velocity waveform.

The maximum shear rate takes place at point 2 which is the point located proximal to the brachiocephalic artery, this is due to the suction created by the brachiocephalic where as discussed earlier in section 3.2, 14 percent of the flow is diverted

throughout the pulsatile cycle, high momentum flow is diverted into the branch and flows in the vicinity of the wall creating a zone with a high velocity gradient and therefore high shear values. Point 3, located between the brachiocephalic and the left common carotid, has the second highest shear rate, this is due similarly to the lower pressure within the left common carotid creating a suction effect.

Point 4, located between the left common carotid and the left subclavian, follows with the third highest shear rate. The high value is similarly due to the suction effect.

Point 6, located within the inner wall at the maximum curvature area, has lower values compared to the other selected locations, this is primarily due to the curvature that leads to low velocity field in that region.

These results are in agreement with suction investigations in viscous fluid mechanics performed by White (1979). Also, the shear rate values found correspond to values previously reported by Friedman *et al.* (1981) and Ku *et al.* (1985). The highest values for the shear rate in our study was 1099 s^{-1} while Ku *et al.* (1985) found values as high as 1171 s^{-1} . These results are a slight improvement compared to the results of the study performed by Shahcheraghi *et al.* (2002) where shear rate reached as high as 4000 s^{-1} .

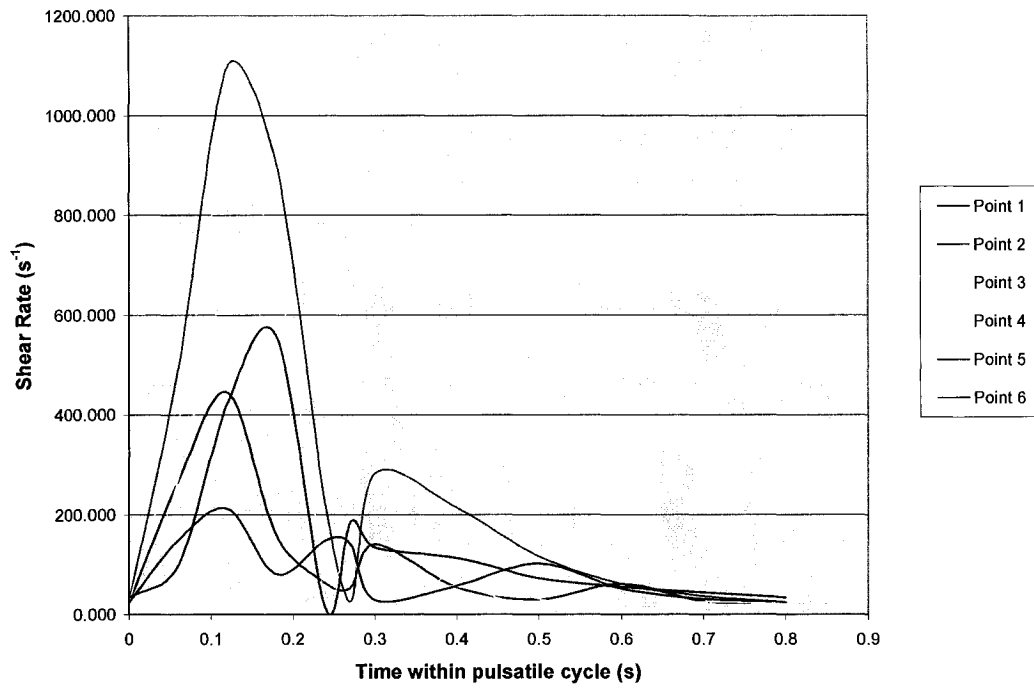


Figure 4.12 Shear rate time history of the different locations studied.

4.5 Discussion

We have performed a numerical study to elucidate the time dependent hemodynamics in an anatomically realistic human aorta, which was reconstructed from magnetic resonance imaging.

Overall, the results have revealed flow patterns that are similar to the ones reported in previous studies (Redkiewicz, 1975; Yearwood and Chandran, 1984, and Shahcheragi *et al.* 2002). Blood flow is skewed towards the outer wall of the aorta and especially in the ascending and descending parts. Similarly and due to curvature, blood flow is highly skewed towards the distal walls of the branches. Pressure is maximum within the outer walls of the aortic arch and the junction with the distal walls of the branches. Wall shear rate magnitude follows a pattern that resembles the inlet velocity waveform throughout the pulsatile cycle. Shear is maximum at a point located proximal to the brachiocephalic artery; this is due to the suction effect created by the lower pressure in the brachiocephalic artery.

What is different in this study is that we have assumed inlet boundary conditions that were derived from recent hemodynamics studies and used a realistic inlet waveform and equivalent blood flow rates. In addition, no flow boundary conditions were imposed at the branches' exits and results revealed that flow distribution was very close to physiological ranges.

Shahcheraghi *et al.* (2002) have assumed that five percent of the total mass flow into or out of each of the three aortic branches while there was no reason to assume that it is constant throughout the cycle and that it is indeed equal for all the three branches. In their conclusion, they wrote: "A very important question for future studies is the proper distribution of total flow into the branches during the cardiac cycle". We found that the resultant flow distribution into the branches agreed better with measured physiological values performed by Bell *et al.* (1965) compared to the Shahcheraghi *et al.* (2002) where percentage variations were between 25% (for the LCC) and 120% (for the brachiocephalic). This is probably the major contribution of this section of the thesis.

Singh (1974), and Yao and Berger (1975) described the development of the flow in curved pipes. When the fluid first enters the pipe, the central core of the flow is not

influenced by the viscous effects, these effects are confined to a thin layer near the walls. This boundary layer develops initially like that in a straight pipe. Therefore, immediately downstream of the entrance the flow consists of two regions:

- A central core in which the centrifugal force, due to the curved motion of the fluid is balanced by a pressure gradient force directed toward the center of curvature.
- A thin boundary layer in which there is a balance between the viscous and the inertial forces.

The displacement effect of the growing boundary layer accelerates the flow in the core and induces a secondary flow from the inner wall to the outer wall of the curvature. Curvature therefore induces a secondary flow, with slower moving fluid in the boundary layer on the wall moving toward the inner wall, and faster moving fluid in the core moving toward the outer wall. The combination of these two effects result in high momentum flow located closer to the inner wall in low bend angles mainly due to the resulting increase in pressure at the inner wall.

It is interesting to note that the hemodynamics of the ascending part of the aorta is highly complex in nature: As the flow gains momentum through maximum acceleration, the flow is blunt with high momentum flow slightly located towards the inner wall. As the flow further gains momentum towards peak systole and with the effect of viscosity, the high momentum flow is located within the central portion of the cross section. This is possibly due to the balance between the centrifugal force due to the curvature directed toward the outer wall and the pressure gradient force directed toward the inner wall. During maximum deceleration, the momentum of the flow is reduced along with the pressure gradient and flow is allowed to start its return towards the outer wall. During flow reversal, the flow continues its return towards the outer wall and hence the creation of Dean like secondary flow vortices.

Throughout the flow cycle, the flow in the ascending part of the aorta is therefore very complex and doesn't resemble at all times the typical flow in curved tubes. This is due to the altered geometry, the tapering of the cross section going downstream, the change in the radius of curvature, the presence of the branches, and the flow pulsatility.

The results of this thesis also gave great insight with respect to the time dependent distribution of shear stress; they have shown that high shear stress regions occur within the distal walls of the branches' junction to the aortic wall and within the outer wall of the ascending aorta. Results also show that low shear stress region localize in the proximal walls of the branches, in the downstream section of the aortic arch, and within a large portion of the ascending aorta.

As to the time dependence distribution of pressure, results show that high pressure zones occur in three stagnation regions which are located within the distal walls of the branches' junction to the aortic arch. Low pressure regions are located within the proximal walls of the branches at the junction within the outer wall of the aorta. Overall, the lowest pressure values are observed downstream of the branches, within the downstream portion of the inner wall of the aortic arch, and in a large portion further downstream within the descending aorta.

As discussed earlier, Rodkiewicz (1975) found that atherosclerosis develops in both the aortic arch within the vicinity of the branches, and in the inner wall of the aortic arch at the maximum curvature area.

In our model, the reported regions of atherosclerosis development (distal walls of the branches) may be related to high shear stress variations. Atherosclerosis development in the proximal walls of the branches may be related to high shear stress. Early atherosclerosis development within the inner walls of the aortic arch may be related to low shear stress values.

It has been suggested in the past that arterial wall thickening may be a process through which the artery decreases its luminal area to increase pressure and shear (Friedman, 1990). In the descending aorta, we found shear and pressure to be lower with respect to the rest of the aorta, this may be a reason why aortic coarctation is usually found in that area. The aortic wall in that region may possibly be responding to the lower pressure and shear values by decreasing its lumen area to consequently increase shear and pressure to levels comparable to the rest of the aorta as was suggested by Friedman (1990).

High shear stress and high pressure are also known to cause damage to the endothelial cells; we found that the outer wall of the ascending aorta and the distal walls of the branches within the aortic arch are characterized by high shear and high

pressure at systole. This may be linked to aneurysm growth and dissection which generally develop starting at these locations.

4.6 Study Limitations

Eventhough the study was performed with a realistic geometrical model, there are limitations that are associated with magnetic resonance data acquisition, the limited spatial resolution used, errors associated with the 3-D reconstruction of the model (Moore *et al.* 1998), and additional errors associated with the manual global structure corrections using Pro/Engineer.

Rigid walls assumption was used to solve for the computational problem while it is known that the arterial wall and especially that of the aorta is compliant. However, Lighthill (1975) and Berger *et al.* (1983) have determined through numerical analysis that eventhough wall compliance is particularly important in determining the pulse wave propagation and determining the local pressure gradient in curved tubes, they found that it had little effect on the fluid motion.

The movement of the aorta resulting from its attachment to a beating heart was ignored. It is not clear how the movement of the aorta may affect the results.

In addition, the aortic sinuses and the valve leaflets were not included in the geometry and consequently their effects on the flow field and pressure distribution was not taken into account.

Because of limitations in the numerical code used, we couldn't assess oscillatory shear stress index which was correlated to atherosclerosis and intimal thickening (Ku *et al.*, 1985).

We have also assumed Newtonian fluid. Numerical simulations using non-Newtonian blood models have proven only modest changes compared to Newtonian blood models and therefore suggest that Newtonian simulations provide adequate estimates in large and medium size arteries (Low *et al.*, 1993; Dutta and Tarbell, 1996). These studies indicate that the assumption of a Newtonian that we have taken will produce little change in the hemodynamics results.

Chapter 5: Effects of Inlet Flow Conditions on Flow Results

5.1 Inlet Flow Conditions in the ascending aorta

Bogren and Buonocore (1999) used four-dimensional magnetic resonance velocity mapping to study normal flow patterns in the aortic arch in sixteen normal subjects. Two groups were studied, one young group with an average age of 31 years and a second group with elderly people with an average age of 72 years. Blood flow was never found to be perfectly parabolic and peak systolic velocities were found to be higher in young subjects compared to the elderly.

Even with the recent technological advancement in medical imaging and particularly magnetic resonance imaging, it is still difficult today to assess accurately the flow conditions within the ascending aorta (Kvitting *et al.*, 2004). Obtaining accurate information on the flow conditions within the ascending part is key to modeling realistic flow conditions within the human aorta. We therefore decided to investigate blood flow in our aortic model using two new inlet velocity profile boundary conditions and compare the results obtained in the previous chapter using the Poiseuille inlet profile.

The findings should help assess the effects of the velocity inlet boundary conditions on the hemodynamics in the aorta and its importance in numerical modeling.

The two inlet velocity profiles are:

- A flat or “plug” inlet velocity profile equivalent to a flow rate of 5l/min and a peak systolic flow rate of 20 l/min. The peak systolic velocity is 0.675 m/s.
- A skewed (towards the outer wall) velocity profile equivalent to a flow rate of 5l/min and a peak systolic flow rate of 20l/min skewed towards the outer wall: The peak systolic velocity is 1.9 m/s.

The following study will enable us to assess the effects of the inlet velocity profiles on velocity, pressure, and shear distributions within the aortic model. It will also enable us to determine whether the flow within the aorta is a flow dominated or geometry dominated field. In other words, which is more dominant and plays the

major role in determining the flow conditions: is it the inlet conditions or the geometry?

5.2 Influence of inlet boundary conditions on Velocity Results

5.2.1 Overview

Figures 5.1 and 5.2 respectively show the axial velocity within the central plane of the aorta at peak systole for the case of the skewed inlet profile and the plug inlet profile. One can notice that because of the complexity of the model, the velocity is highly skewed and changes in distribution from one location to the other.

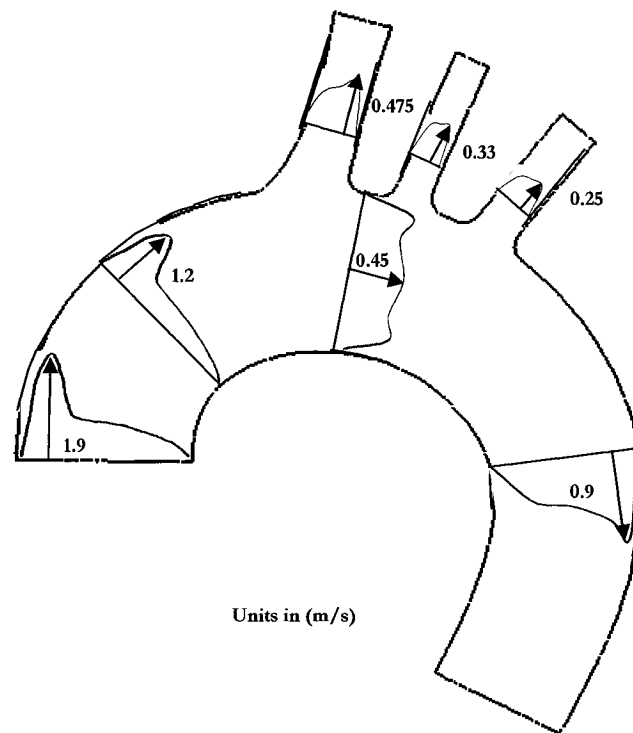


Figure 5.1 Axial Velocities at the selected cross sections within the central plane of the aorta at peak systole for the case of the skewed inlet velocity profile. The units are in m/s.

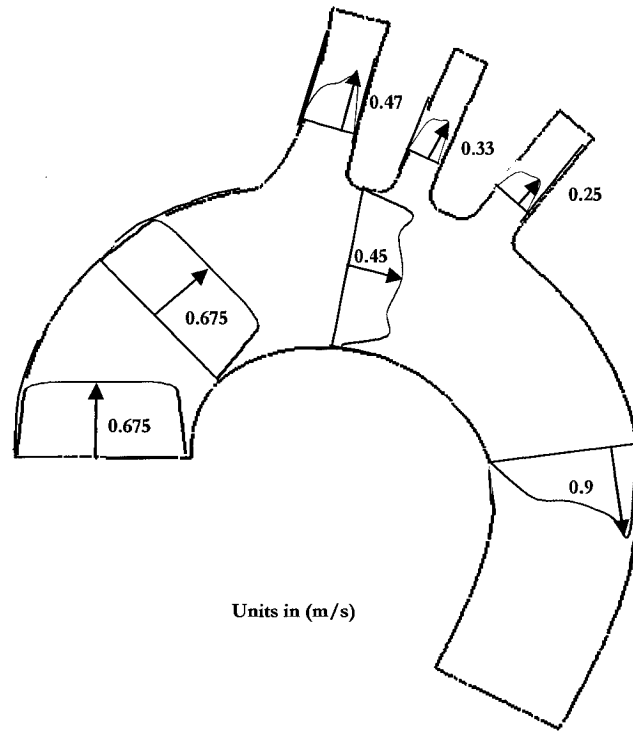


Figure 5.2 Axial Velocities at the selected cross sections within the central plane of the aorta at peak systole for the case of the flat inlet velocity profile. The units are in m/s.

Similarly to the previous chapter, the flow results of six different cross sections will be displayed as previously illustrated on figure 4.2: Six axial cuts or slices within the aortic model, three within the main aorta where one is taken within the ascending aorta, one within the aortic arch between the brachiocephalic artery and the left common carotid, and the third slice within the descending aorta. The three others are respectively within the brachiocephalic artery, the left common carotid, and the left subclavian artery. Similar to the previous plots, the color contour plot shows the out of plane velocities and the vector plot shows the secondary flow velocities. The results are again displayed such that the view point is from a distal position with the outer wall positioned at the left and the inner wall at the right. For this part of the study, however, results according to the three inlet boundary conditions will be displayed which are: the Poiseuille, the plug, and the skewed inlet profiles.

5.2.2 Velocity Results

Ascending Aorta:

Figure 5.3 shows the blood flow distribution for the three inlet profiles within the ascending aorta. Blood velocity distribution is similar within the ascending aorta during the early systolic phase. As blood reaches peak systolic, one can notice that high momentum flow is considerably skewed towards the outer wall in the case of the skewed inlet flow and equally distributed in the case of plug flow as expected. As the blood is decelerating and throughout the diastolic phase, primary flow loses momentum until it reaches maximum retrograde value at peak reversal. Strong secondary flow, from the outer to the inner wall, is also induced by the curvature as in a simple curved pipe flow. It is interesting to note that during maximum deceleration and peak diastole, secondary flow forms complex patterns where flow direction is reversed going from the outer wall into the inner wall and going from the arterial wall into the lumen. One should also note that flow patterns during peak systole and maximum acceleration are very similar independent of the inlet boundary conditions and especially when comparing results of the Poiseuille and skewed inlet conditions.

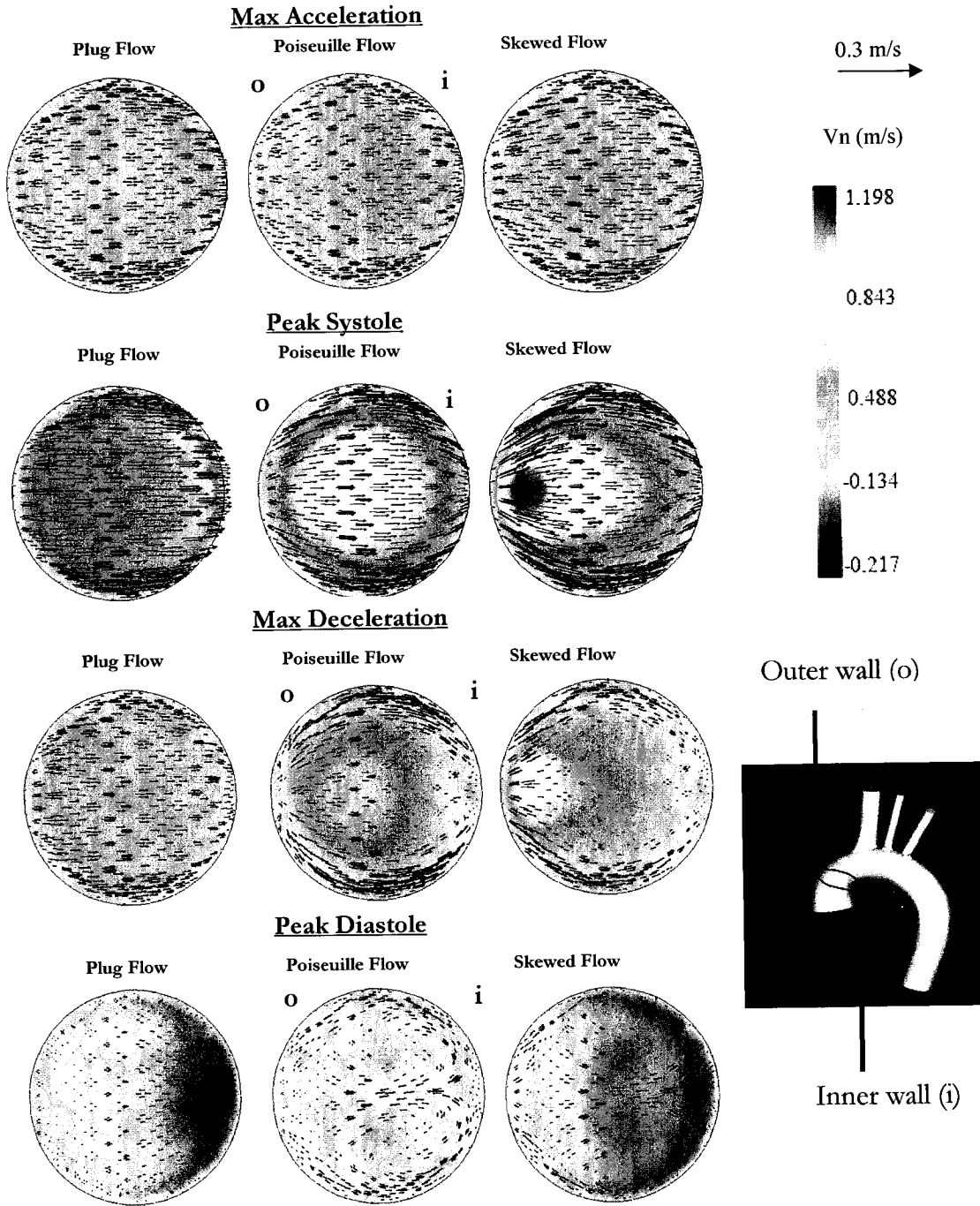


Figure 5.3 Velocity distributions within the ascending aorta for the three different inlet profiles, at the four time points of interest. Looking at the cross section, the outer wall of the aorta is located at the left and the inner wall at the right.

Aortic Arch:

Figure 5.4 shows the velocity distribution within the aortic arch for the three inlet profiles. As blood picks up momentum, high momentum flow is localized within the outer walls as in the case of curved tubes. As blood flow reaches peak systolic, high momentum flow is located within the lateral walls, these particular results have been explained in the previous chapter: High momentum flow localized in the outer wall of the ascending aorta have been diverted into the brachiocephalic artery and high momentum flow within the lateral walls went downstream as found in previous studies. Reverse flow during peak reversal was found within the outer wall of the aortic arch and is likely due to the branches discharging blood back into the aorta. It is interesting to note that results are very similar independent of the inlet flow velocity boundary condition used and that for all four times studied, this may suggest that inlet boundary conditions effects are fading as flow is progressing downstream.

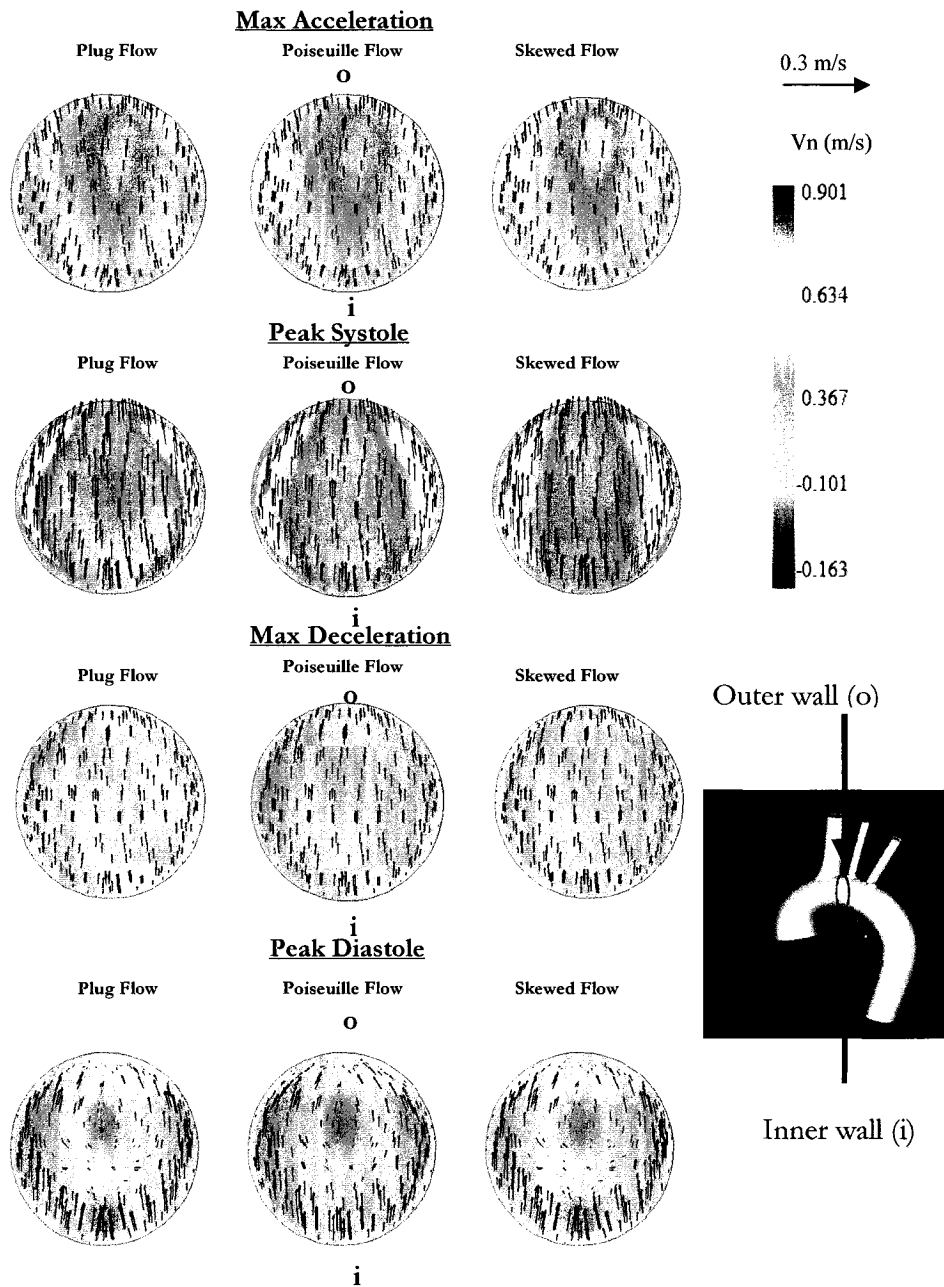


Figure 5.4 Velocity distributions within the aortic arch for the three different inlet profiles, at the four time points of interest. Looking at the cross section, the outer wall of the aorta is located at the top and the inner wall at the bottom.

Descending Aorta:

Figure 5.5 shows the velocity distribution within the descending aorta for the three inlet profiles. The high momentum flow is skewed towards the outer wall as in the case of flow in curved tubes. Secondary flows within the descending aorta form patterns that are similar to the ones observed in the ascending aorta. However, when compared to secondary flow in the ascending aorta, the magnitudes in the descending aorta are significantly lower.

The most important observation is that flow distribution is the same independent of the inlet flow velocity boundary condition used and that for all four times studied, this suggests that inlet boundary conditions effects have faded away as flow progressed downstream away from the ascending aorta.

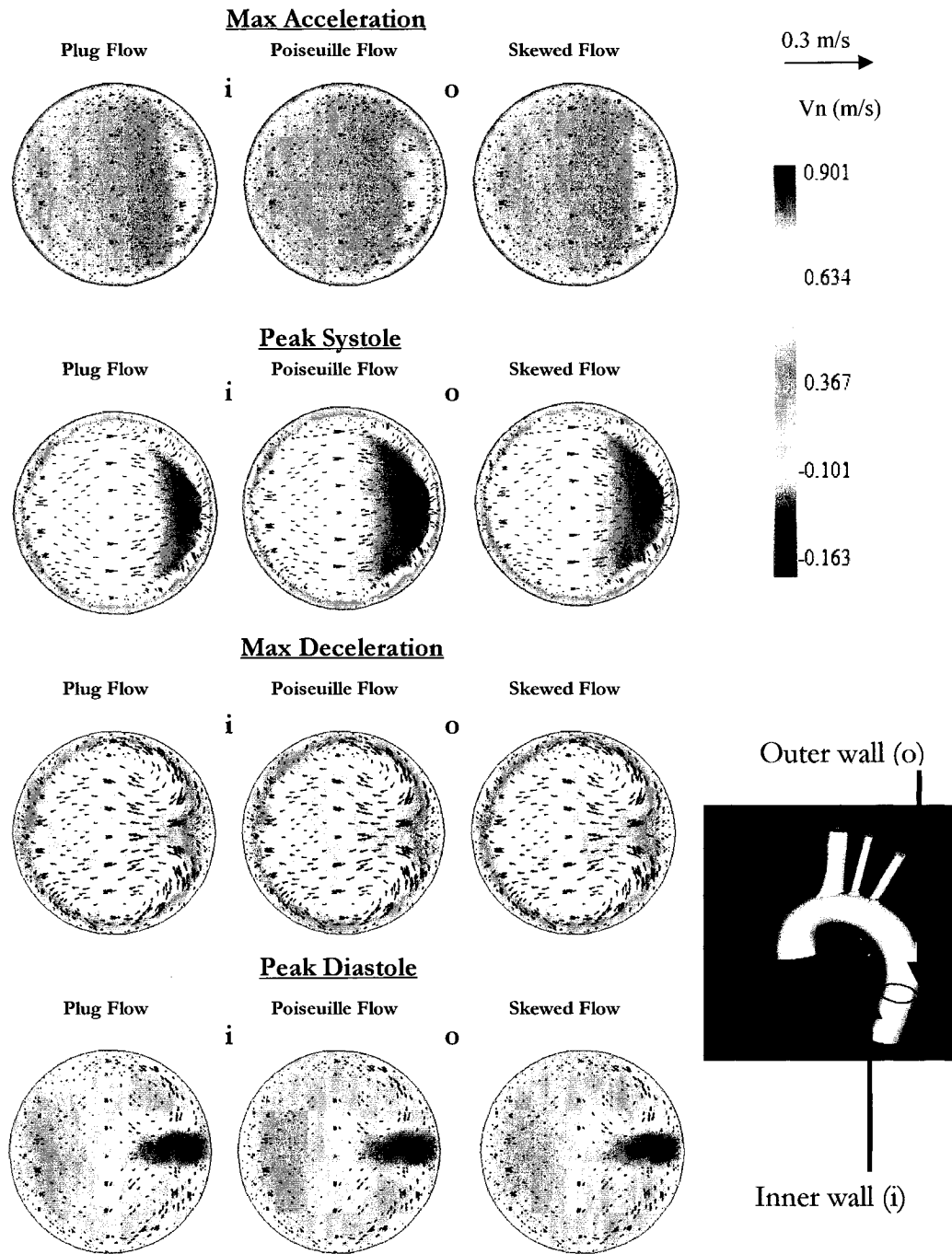


Figure 5.5 Velocity distributions within the descending aorta for the three different inlet profiles, at the four time points of interest. Looking at the cross section, the outer wall of the aorta is located at the right and the inner wall at the left.

Brachiocephalic artery:

Figure 5.6 shows the blood flow velocity distribution within the brachiocephalic artery respectively at maximum flow acceleration, peak systole, maximum deceleration, and peak reversal for the three inlet velocity profiles. The figures are laid out such that the distal wall is at the right while the proximal wall is at the left.

Primary flow is highly skewed towards the distal wall of the artery especially in peak systole where high momentum flow forms a pattern similar to a horseshoe facing the distal wall. As blood gains momentum throughout the systolic phase, secondary flows is mainly directed from the proximal wall to the distal wall. During maximum deceleration, the momentum of the fluid is reduced enough to allow flow to be returned to the proximal wall by the pressure build up in the distal wall. The return of fluid toward the proximal wall continues through peak diastole. There is however an additional secondary flow developing from the proximal arterial wall towards the distal central section which is due to the abrupt area constriction going from the main arch into the brachiocephalic artery.

During peak diastole, the flow is similar for all three inlet velocity profiles: Primary flow is reversed with a nearly axisymmetric profile. Secondary flow, also reversed, is mainly directed from the distal wall towards the proximal wall.

A difference in axial flow is seen in the three different inlet boundary conditions, however, this difference is more difficult to see in the secondary flow.

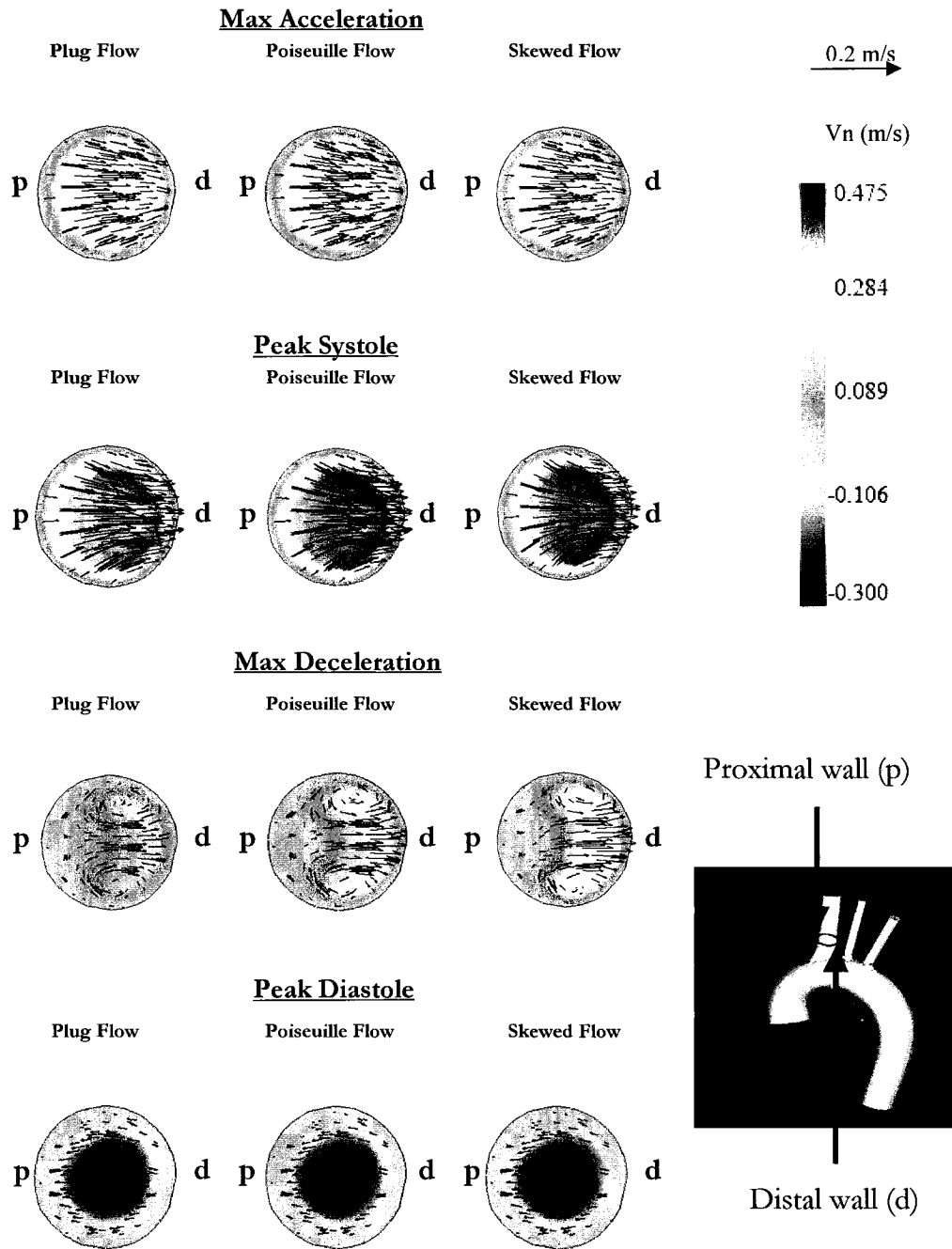


Figure 5.6 Velocity distributions within the brachiocephalic artery for the three different inlet profiles, at the four time points of interest. Looking at the cross section, the distal wall of the branch is located at the right and the proximal wall at the left.

Left Common Carotid:

Figure 5.7 shows the flow velocity distribution within the left common carotid at maximum acceleration, peak systole, maximum deceleration, and peak diastole for the three inlet velocity profiles. Primary flow is skewed towards the distal wall of the artery especially in peak systole where high momentum flow forms a pattern similar to a horseshoe facing the distal wall; it is however not skewed to the levels observed in the brachiocephalic. As blood gains momentum throughout the systolic phase, secondary flows are mainly directed from the proximal wall to the distal wall. During maximum deceleration, the momentum of the fluid is reduced enough to allow flow to be returned to the proximal wall by the pressure build up in the distal wall. The return of fluid toward the proximal wall continues through peak diastole. There is however an additional secondary flow developing from the proximal arterial wall towards the distal central section which is due to the abrupt area constriction going from the main arch into the brachiocephalic artery. Flow patterns during maximum deceleration and peak reversal are also similar.

It is interesting to note that flow distribution is the same no matter what inlet velocity profile is used, this is a clear indication that the effects of the inlet velocity conditions have faded away as flow progressed downstream and away from the ascending aorta.

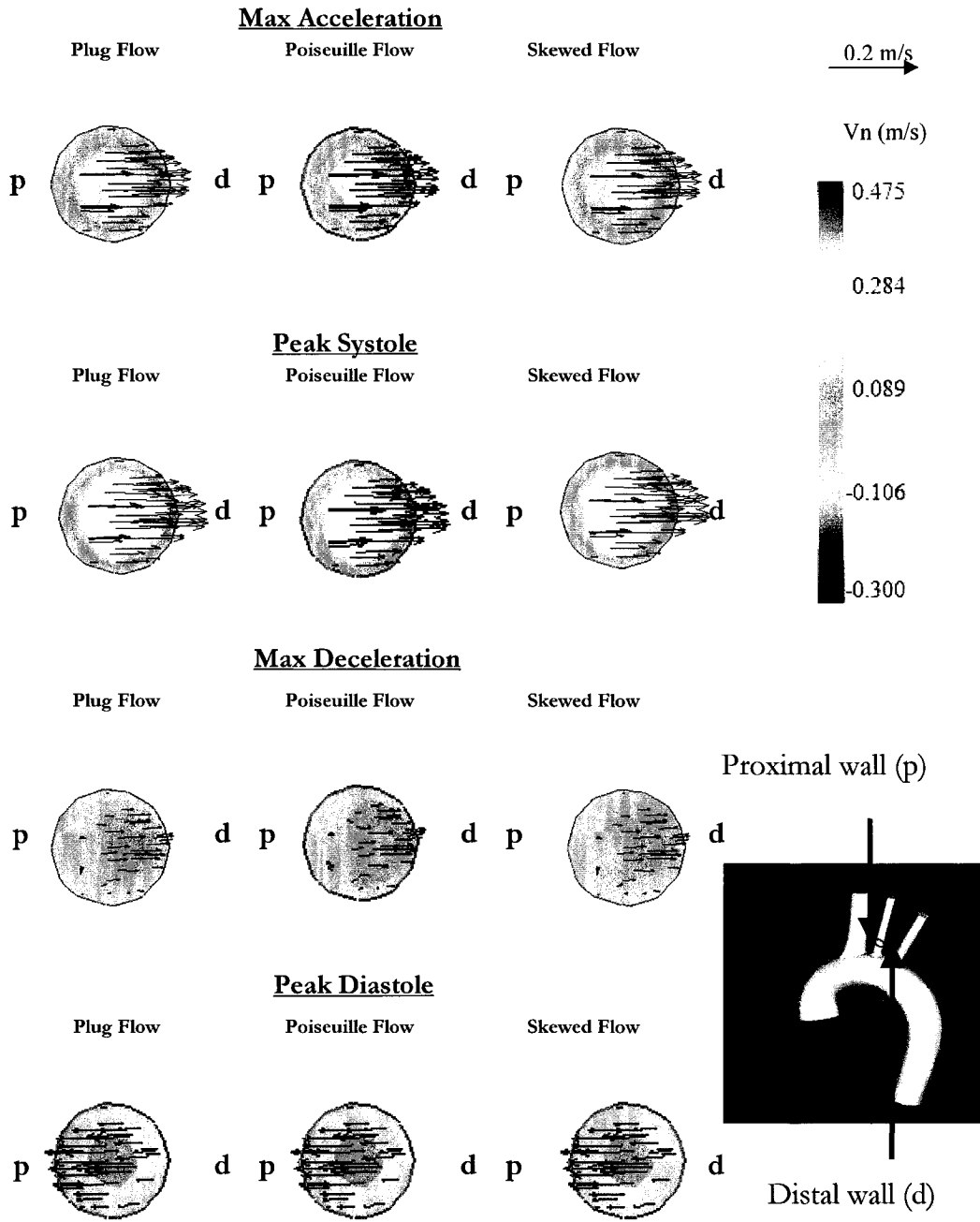


Figure 5.7 Velocity distributions within the left common carotid for the three different inlet profiles, at the four time points of interest. Looking at the cross section, the distal wall of the branch is located at the right and the proximal wall at the left.

Left Subclavian Artery:

Figure 5.8 shows the flow velocity distribution within the left subclavian artery at maximum acceleration, peak systole, maximum deceleration, and peak diastole for the three inlet velocity profiles. Similarly, the flow distributions are the same no matter what inlet velocity profile is used.

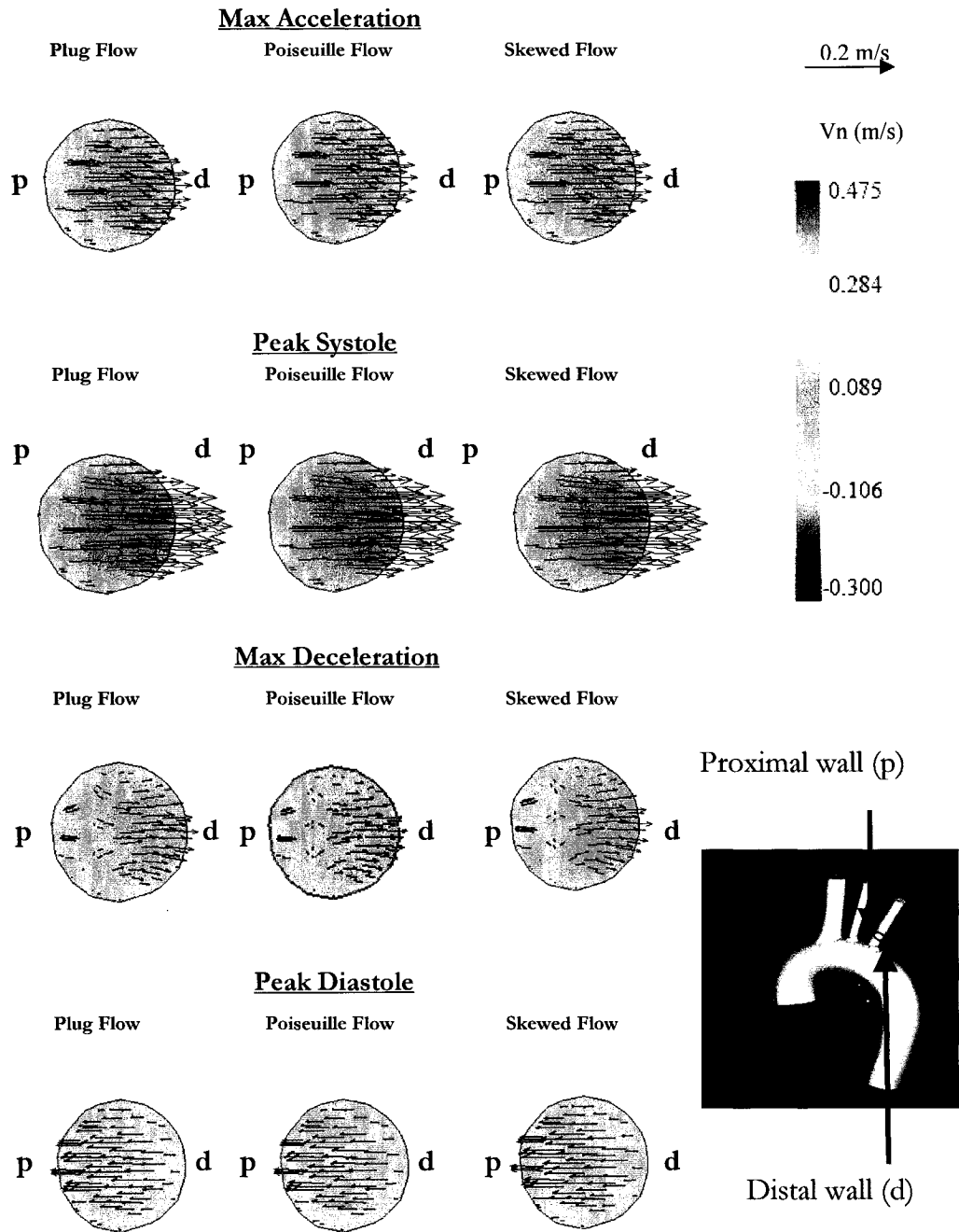


Figure 5.8 Velocity distributions within the left subclavian artery for the three different inlet profiles, at the four time points of interest. Looking at the cross section, the distal wall of the branch is located at the right and the proximal wall at the left.

5.3 Effect of inlet boundary conditions on flow distribution into the branches

Flow rates for each time step within the pulsatile cycle were compiled for the inlet and for the four exit boundaries (brachiocephalic, left common carotid, left subclavian, and descending aorta) and were summed. Table 5.1 shows the value for each exit boundary and their percent variation with respect to the measured values by Bell *et al.* (1965) discussed in section 4.2.

Flow distribution within the aorta (%)						
	Plug Inlet		Poiseuille Inlet		Skewed Inlet	
	Result	% variation	Result	% Variation	Result	% Variation
Descending	78.57	0.73	77.42	0.74	76.68	1.69
Brachiocephalic	12.10	10.02	13.59	23.54	14.39	30.77
LCC	3.43	14.25	3.29	17.75	3.22	19.49
LSC	5.69	18.66	5.50	21.43	5.52	21.14
Average % Variation (Bell <i>et al.</i> 1965)		10.92		15.87		18.27

Table 5.1 Flow distribution within the aorta for the three different inlet velocity profiles. Percentage variations have been tabulated with respect to the measured values by Bell *et al.* (1965) discussed in section 4.2

Statistical analysis of the flow distribution results revealed a value of $p=0.6528$ using a paired one-way Anova Friedman test which indicates that the inlet velocity boundary has little influence on the flow distribution into the branches.

The geometry of the aortic arch therefore plays the dominant role in dictating blood distribution within the human body. This may suggest that the aortic arch geometry is not only a passive channel for blood distribution but is in fact actively making sure that blood is distributed properly independent of the cardiac input and the velocity inlet profile which may change with age as discussed earlier.

5.4 Influence of inlet boundary conditions on Pressure Results

The wall pressure contours are presented in figures 5.9 and 5.10. The pressure values were converted from the output units in Pascal into millimeter of mercury (mmHg) for ease of interpretation. As the flow picks up momentum, overall pressure values increase within the aorta and decrease with flow reversal and during diastole.

A high pressure region is seen at the distal end of the branch ostia created by the redirection of the bulk flow by the branch artery connections. Another high pressure region is the outer wall within the ascending aorta, where the sharp curvature redirects the high momentum flow.

Low pressure region is seen at the proximal walls of the branches near the branch ostia because the bulk flow is skewed to the outer wall. Overall, the lowest pressure values are observed downstream of the branches, within the downstream portion of the inner wall of the aortic arch, and in a large portion further downstream within the descending aorta.

What is most interesting to note is that the change in the inlet velocity profile has a slight effect on pressure distributions: The highest variation was observed within the ascending aorta during peak systole where peak pressure went from 131 in the case of Poiseuille inlet to 135 mmHg in the case of skewed profile: A variation that represents a 3% increase.

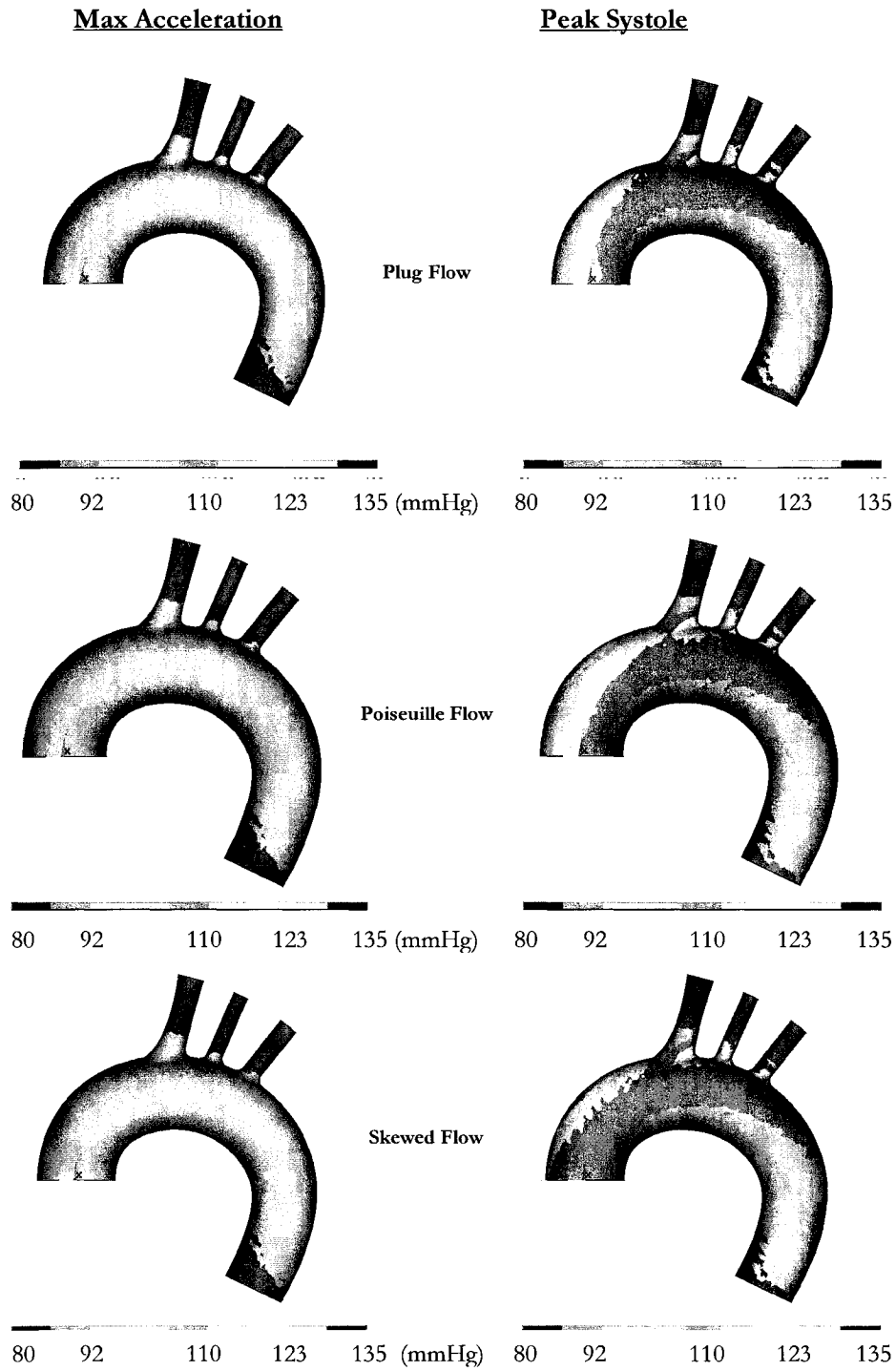


Figure 5.9 Pressure distributions within the aortic wall for the three different inlet profiles, at maximum acceleration and peak systole. The units are in mmHg. 1 mmHg is equal to 133.3 Pa.

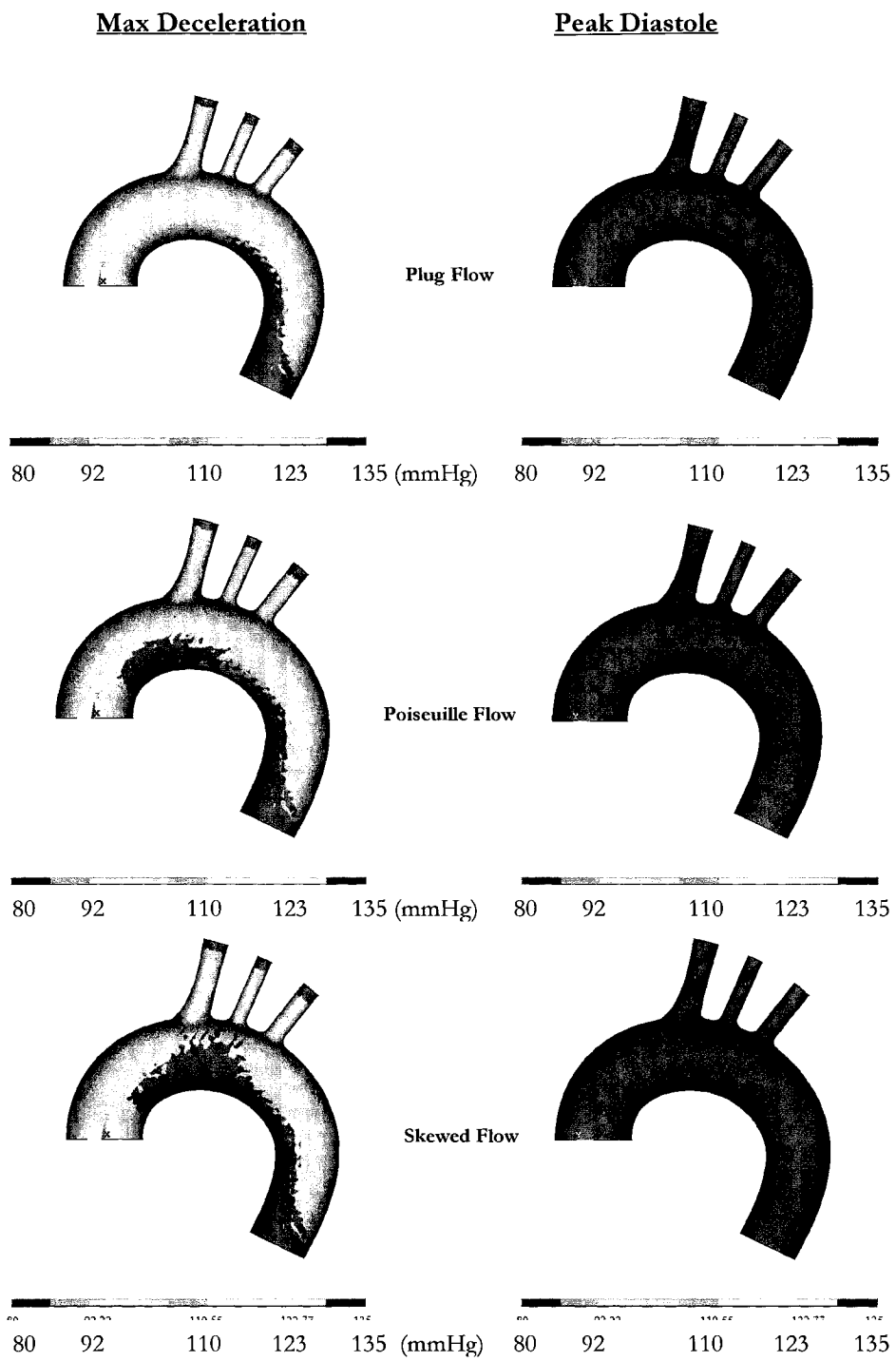


Figure 5.10 Pressure distributions within the aortic wall for the three different inlet profiles, at maximum deceleration and peak diastole. The units are in mmHg. 1 mmHg is equal to 133.3 Pa.

5.5 Influence of inlet boundary conditions on Shear Results

Figure 5.12 shows the time history of the shear rate in six different locations within the aortic arch. These locations as illustrated in figure 5.11 are the same locations used in section 4.4 for the shear rate study.

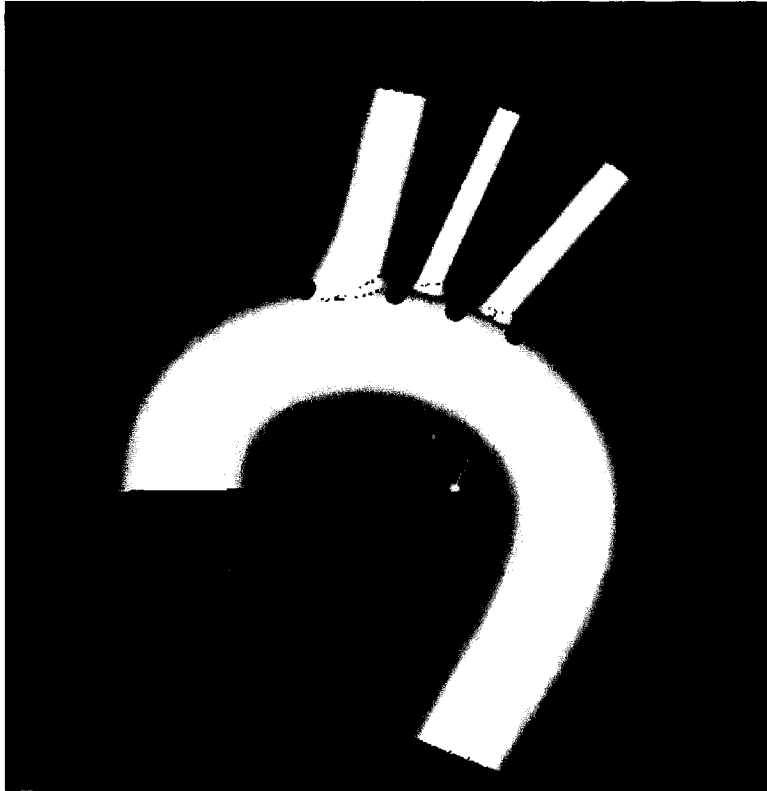


Figure 5.11 Locations for shear rate time history investigation.

Similar to the findings in section 4.4, the wall shear rate magnitude for the three cases and throughout the pulsatile cycle follows a pattern that resembles the inlet velocity waveform. As the flow is accelerating, shear rate values increase to reach maximum values. As the flow is decelerating within the end of the systolic phase, shear rate values decrease and stay at relatively low levels throughout the diastolic phase. Point 1, which is located within the outer wall of the ascending aorta, is a fine example for all inlet velocity profiles studied. As you can see from figure 5.12, its shear rate history closely resembles that of the inlet velocity waveform.

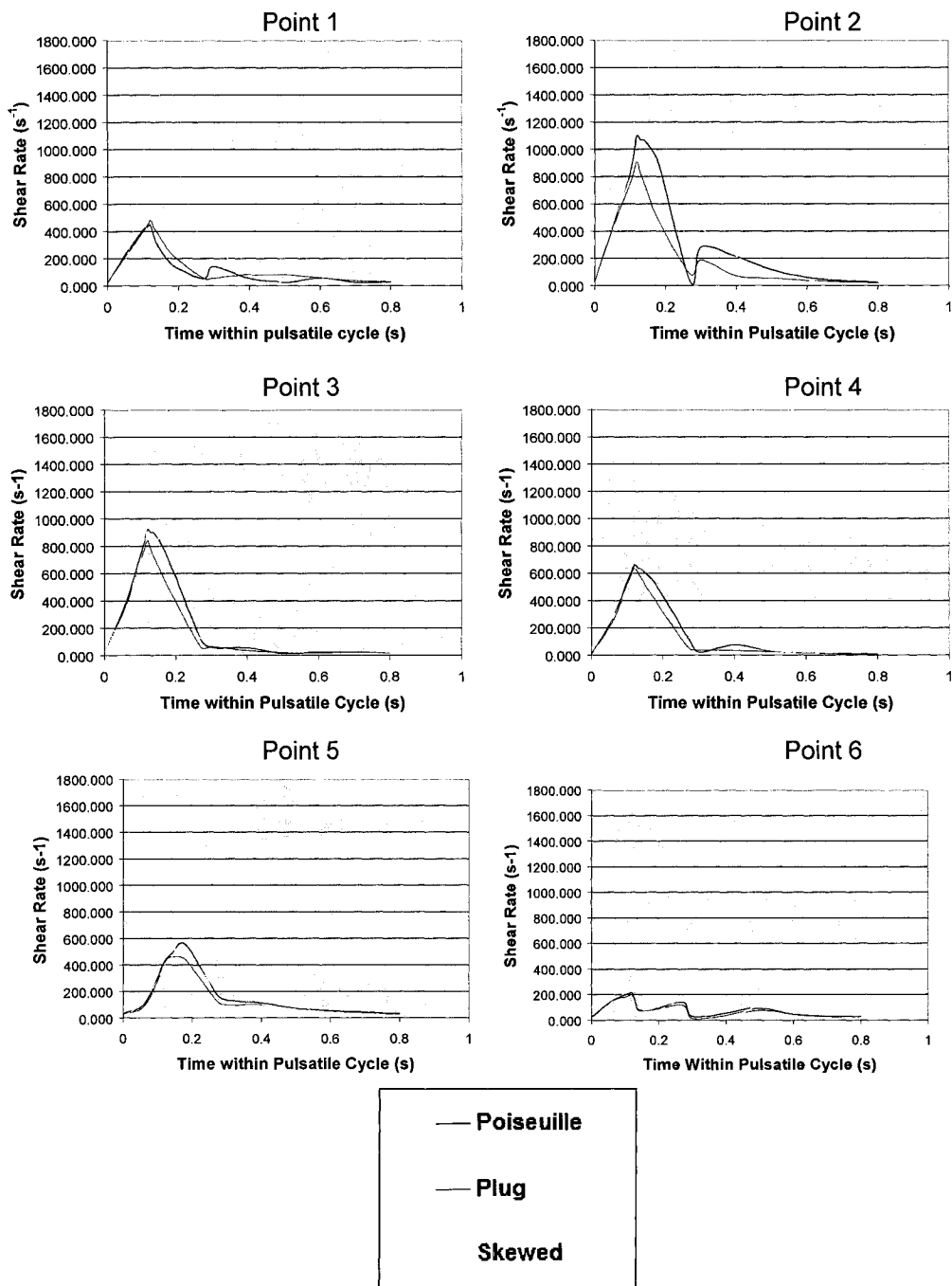


Figure 5.12 Shear rate time history at selected points within the aortic arch.

Overall, the pattern of temporal shear distribution is similar in all cases independent of the inlet velocity profile. The magnitude of shear is significantly different at the first two points studied. Further downstream, the difference is less significant.

In the case of the skewed inlet velocity profile, high momentum flow is located near the outer wall of the ascending aorta, this may explain the higher shear rate values found in this case compared to the Poiseuille and the plug flow at point 1.

The maximum shear rate takes place at point 2 which is the point located proximal to the brachiocephalic artery, this is due to the suction created by the brachiocephalic where as discussed in section 4.2, 14 percent of the flow is diverted throughout the pulsatile cycle. Similarly to the results of point 2, the shear rate values are higher for the case of skewed inlet velocity profile.

It is interesting to note that once we reach point 3, located between the brachiocephalic and the left common carotid, results are similar and vary slightly.

This is, again, a clear indication that the effects of the inlet velocity fade away as the flow progresses downstream; the geometry becomes the dominating factor in determining the velocity distribution and consequently the shear rate distribution as well.

5.6 Discussion

We have performed this numerical study to investigate the effects of inlet velocity profile on velocity, pressure, and shear distributions in the aortic model and assess its importance in numerical modeling.

The results have revealed flow patterns that are similar to the ones reported in previous studies independent of the inlet velocity profile used (Redkiewicz, 1975; Yearwood and Chandran, 1984, and Shahcheragi *et al.* 2002).

The results have shown that altering the inlet velocity profile led to variations in the velocity, pressure, and shear distributions within the ascending aorta. The effects of the inlet velocity profile however faded away as the flow progressed downstream within the aortic arch and into the branches. This suggests that the geometry is possibly the major determinant in velocity, pressure, and shear distribution.

These findings may also suggest that the complex geometry of the aorta may play an important and active role in making sure that proper blood flow is distributed at the right proportions to the different parts of the human body.

Myers *et al.* (2001) performed steady state flow simulations ($Re = 500$) and pulsatile flow simulations ($\alpha = 1.82$ and $Re = 233$) on an anatomically realistic model of a human right coronary artery using three different inlet velocity profiles. They found that the change in the inlet velocity profile did not produce significant changes in the arterial velocity and wall shear stress patterns. Compared to our study, the effect of the inlet velocity profile fades away much faster in Myers *et al.* (2001) study: This is mainly due to the smaller dimensions of the right coronary artery compared to the aorta, the lower Reynold's number ($Re = 233$) and the lower Womersley number ($\alpha = 1.82$) used by Myers *et al.* (2002).

We found that the change in velocity inlet profile had a significant effect on the shear magnitude within the ascending aorta. Shear magnitude due to the skewed profile was higher than the magnitude found using a Poiseuille and flat profile. If shear stress magnitude is the determining factor in the genesis and development of atherosclerosis, then velocity magnitude and its spatial distribution may have an effect on atherosclerosis development. However, if temporal distribution of shear is

the determining factor then our findings are not conclusive and further studies are needed.

As discussed in section 5.1, Bogren and Buonocore (1999) used four-dimensional magnetic resonance velocity mapping to study normal flow patterns in the aortic arch in normal subjects. Peak systolic velocities were found to be higher in young subjects compared to the elderly: This may either be the consequence of a reduced hemodynamical cardiac output with age or that the body may be adjusting its cardiac output velocity profile as a result of changing hemodynamic conditions or arterial wall compliance with age.

We may argue that the body adjusts its cardiac output by changing the velocity profile from a highly tapered profile into a plug profile to reduce the blood pressure applied on the outer wall of the ascending aorta. High pressure within that region has been linked to aneurysm formation and rupture as discussed in section 5.5, decreasing the pressure may therefore decrease the likelihood of developing aortic disease in that region. The regulation of arterial blood pressure is accomplished by negative feedback systems incorporating pressure sensors called baroreceptors and located in the aortic arch. These receptors are sensitive to the rate of pressure change as well as to the steady or mean pressure and are responsible for heart rate and blood pressure control by affecting the body to cause vasoconstriction or vasodilatation, change of heart rhythm, and change in the cardiac stroke volume by modifying ventricular contractility.

What is really interesting to note however is that we have found that inlet velocity profile is of great importance when modeling the flow in the ascending aorta. This has serious implications for valve replacement, where the orientation of the prosthetic valve implanted may alter the hemodynamics of the ascending aorta. Presently, recommendations as to the orientation of the prosthetic valve have not been set and vary from one health center to the other. It will be interesting to study the effect of the orientation of prosthetic valves on the hemodynamics in the ascending aorta especially that it is known that bicuspid patients are more likely to develop dilatation of the aorta, aneurysms, and dissection (Fedak *et al.* 2002).

5.7 Study Limitations

The limitations for this section of the study are the same as the ones mentioned in section 4.7. Eventhough the study was performed with a realistic geometrical model, there are limitations that are associated with magnetic resonance data acquisition, the limited spatial resolution used, errors associated with the 3-D reconstruction of the model (Moore *et al.* 1998), and additional errors associated with the manual global structure corrections using Pro/Engineer.

Rigid walls assumption was used to solve for the computational problem while it is know that the arterial wall and especially that of the aorta is compliant. However, Lighthill (1975) and Berger et al. (1983) have determined through numerical analysis that eventhough wall compliance is particularly important in determining the pulse wave propagation and determining the local pressure gradient in curved tubes, they found that it had little effect on the fluid motion.

The movement of the aorta resulting from its attachment to a beating heart was ignored. It is not clear how the movement of the aorta may affect the results. In addition, the aortic sinuses and the valve leaflets were not included in the geometry and consequently their effects on the flow field and pressure distribution was not taken into account.

Because of limitations in the numerical code used, we couldn't assess oscillatory shear stress index which was correlated to atherosclerosis and intimal thickening (Ku *et al.*, 1985).

We have also assumed Newtonian fluid. Numerical simulations using non-Newtonian blood models have proven only modest changes compared to Newtonian blood models and therefore suggest that Newtonian simulations provide adequate estimates in large and medium size arteries (Low *et al.*, 1993; Dutta and Tarbell, 1996). These studies indicate that the assumption of a Newtonian that we have taken will produce little change in the hemodynamics results.

Chapter 6: Contributions and Conclusions

As stated earlier, the aorta is the primary artery of the circulatory system, delivering oxygenated blood to all other arteries except those of the lungs and is a major site for arterial disease and despite the clinical importance of the aorta, relatively little is known about its hemodynamic features due in part to the difficulty of studying blood flow in this artery.

Most studies in hemodynamics have focused instead on coronary arteries, abdominal aortas, carotid bifurcations, and cerebral arteries using realistic models or simplified geometries such as bifurcations and curved tubes. Recently, however, numerical and experimental studies have been performed using realistic models of three dimensional reconstructions of aortic arches including the aortic branches.

This study is a continuation of the recent efforts in elucidating blood flow patterns in the human aortic arch and presents a numerical analysis on the hemodynamics of the aorta with a focus on velocity, pressure, and shear stress distributions.

We were able to use clinical magnetic resonance imaging data and reconstruct an anatomically realistic model of the human ascending aorta, a model that can be used for numerical simulations. In addition, we have obtained mesh independence for shear stress which is usually the hardest to get (Prakash and Ethier, 2001).

The anatomically realistic geometry along with appropriate boundary conditions have enabled us to obtain flow distribution which agreed better with measured physiological values (Bell *et al.*, 1965). This was a major improvement compared to the latest numerical study performed by Shahcheragi *et al* (2002).

We were able to investigate the influence of the inlet velocity profile on the hemodynamics in the model using three different profiles, a Poiseuille, a flat, and a skewed profile: We found that the inlet velocity profile affected the hemodynamics within the ascending aorta, those effects however faded as we moved downstream within the aortic arch, the branches, and the descending aorta. This suggests that in order to accurately study the hemodynamics of the ascending aorta, one needs accurate flow conditions which has eluded researcher so far. This may also suggest that numerical studies to design prosthetic valves for valve replacement or covered stents to treat ascending aortic aneurysms may not be suitable unless further studies

are performed to accurately determine the hemodynamics conditions within the outflow tract of the left ventricle. This is mainly why expensive *in-vitro* set-ups using pulse duplicators are still the only acceptable way to test prosthetic valves.

The change of inlet velocity profile had little effect on the hemodynamics in the aortic arch, the branches, and the descending aorta and suggests that the geometry is the major determinant of the hemodynamic conditions. It may possibly further suggest that the aorta is not only a passive tract for the distribution of oxygen rich blood into the body but that it does play an active role, thanks to its geometry, to make sure blood is distributed at the right proportions to the different part of the body.

Future work should also include the use of fluid structure interaction (FSI) to better simulate *in-vivo* conditions: FSI is the coupling of unsteady fluid flow (blood) and structure (arterial wall) motion, and is an important field of computational mechanics gaining popularity in the field of cardiovascular biomechanics.

The use of FSI will enable the inclusion of arterial wall compliance to study its effect on the hemodynamics in the aorta and better design prosthetic devices, such as prosthetic valves and stents.

References

- Advanced Medical Imaging Laboratory website (2005), gallery of medical illustration section: www.ctisus.org/gallery/vascular_aortic_pathology.html
- American Heart Association website (2005): www.americanheart.org
- Ansys website, Theory Manual, Chapter 5, Section 1 (2005): www.ansys.com
- Asakura, T., Karino, T. (1990). Flow Patterns and Spatial Distribution of Atherosclerotic Lesions in Human Coronary Arteries. *Circ. Rescan.* Vol. 66, p. 1045-1066.
- Bard, P. (1956). Medical Physiology. C.V. Mosby, Toronto, Ontario.
- Bell, G., Davidson, J.N., and Scarborough, H. (1965). Textbook of Physiology and Biochemistry, 6th ed. E & S Livingston, Edinburgh.
- Berger, S.A., Talbot, L. (1983). Flow in Curved Pipes. *Ann. Rev. Fluid. Mech.*, Vol. 15, p. 461-512.
- Bogren, H.G. and Buonocore M.H. (1999). 4D Magnetic Resonance Velocity Mapping of Blood Flow Patterns in the Aorta in Young vs. Elderly Normal Subjects. *J.Magn. Reson. Imag.*, Vol. 10, p. 861-869.
- Caro, C.G., Pedley, J.G., Shroter, R.C., Seed, W.A. (1978). The Mechanics of Circulation. Oxford University Press, Oxford.
- Cedars-Senai Medical Center website (2004), heart center section: www.csmc.edu/3866.html
- Chandran, K.B. (1993). Flow Dynamics in the Human Aorta. *J. Biomech. Eng.*, Vol. 115, p. 611-616.
- Chandran, K. B. (1997). Flow Dynamics in the Human Aorta: Techniques and Applications. In Biomechanic Systems Techniques and Applications. CRC Press, Boca Raton, FL, Chapter 5, p. 1-25.
- Constantinides, P. (1965) Experimental Atherosclerosis. p. 14-24. Elsevier. New York.
- Davies, P.F. (1995). Flow-mediated Endothelial Mechanotransduction. *Physiol Rev.*, Vol. 75, p. 519-560.
- Davies, P.F., Barbee, K.A., Volin, M.V., Robotewskyj, A., Chen, J., Joseph, L., Griem, M.L., and Barakat, A.I. (1997) Spatial Relationships in Early Signaling

- Evens of Flow-Mediated Endothelial Mechanotransduction. *Ann. Rev. Physiol.*, Vol. 59, p. 527-549.
- Dean, W.R. (1927). Note on the motion of fluid in a curved pipe. *Phil. Mag.* Vol. 4, pp. 208-223.
- Dutta, A., Tarbell, J.M. (1996). Influence of Non-Newtonian Behavior of Blood on Flow in an Elastic Artery Model. *J. Biomech. Eng.*, Vol. 118, p. 111-119.
- Dzau, V.J., and Gibbons, G.H. (1993). Vascular Remodeling: Mechanisms and Implications. *J. Card. Phar.*, Vol. 21, Suppl. 1, p. 1-5.
- Ethier, C. R., Prakash, S., Steinman, D. A., Leask, R. L., Couch, G. G. (2000). Steady Flow Separation Patterns in a 45 Degree Junction. *J. Fluid Mech.*, Vol. 411, p. 1-38.
- Fearn, M., Mullin, T., and Cliffe, K. A. (1990). Nonlinear Flow Phenomenon in a Symmetric Sudden Expansion. *J. Fluid Mech.*, Vol. 211, p. 595-608.
- Fedak, P.W.M., Verma, S., David, T.E., Leask, R.L., Weisel, R.D., Butany, J. (2002). Clinical and Pathophysiological Implications of a Bicuspid Aortic Valve. *Circ.* Vol. 106, p. 900-904.
- Freitas, C. J. (1993). Policy Statement on the Control of Numerical Accuracy. *ASME J. Fluids Eng.*, Vol. 115, p. 339-340.
- Friedman, M.H., Hutchins, G.M., and Bergeron, C.B. (1981). Correlation between Intimal Thickness and Fluid Shear in Human Arteries. *Ather.*, Vol. 39, p. 425-436.
- Friedman M.H. (1990). Some Atherosclerosis may be a consequence of Normal Adaptive Vascular Response to Shear. *Ather.*, Vol. 82, p. 193-196.
- Galt, S.W., Zwolak, R.M., Wagner, R.J., and Gilbertson, J.J. (1993). Differential Response of Arteries and Vein Grafts to Blood Flow Reduction. *J. Vasc. Surg.*, Vol. 17, p. 563-570.
- Guyton, A.C., 1960. *Function of the Human Body*. W.B. Saunders, Don Mills, Ontario.
- Guyton, A.C., 1971. *Textbook of Medical Physiology*. W.B. Saunders, Don Mills, Ontario.
- Hamkiotes, C.C., and Berger, S.A. (1988). Fully Developed Pulsatile Flow in a Curved Pipe. *J. Fluid Mech.*, Vol. 19, p. 23-55.

- Hamkioles, C.C., and Berger, S.A. (1990). Periodic Flows through Curved Tubes: The Effect of the Frequency Parameter. *J. Fluid Mech.*, Vol. 21, p. 353-370.
- Hatle, L., 1984. Maximal Blood Flow Velocities – Hemodynamic data obtained noninvasively with CW Doppler. *Ultrasound Med. Biol.*, Vol. 10, p. 225-237.
- Hatle L., Angelse B. (1985). Doppler Ultrasound in Cardiology. Philadelphia: Lea & Febiger.
- Health Central Website (2005): <http://www.healthcentral.com>
- Komai, Y., and Tanishita, K. (1997). Fully Developed Intermittent Flow in a Curved Tube. *J. Fluid. Mech.*, Vol. 347, p. 263-287.
- Krams, R., Wentzel, J.J., Oomen, J.A., Vinke, R., Schuurniers, J.C., De Feyter, P.J., Serruys, P.W., Slager, C.J. (1997). Evaluation of Endothelial Shear Stress and 3D Geometry as Factors Determining the Development of Atherosclerosis and Remodeling in Human Coronary in vivo. *Arterioscler. Thromb. Vasc. Biol.*, Vol. 17, p. 2061-2065.
- Ku, D.N., Giddens, D.P., Zarins, C.K., Glagov, S. (1985). Pulsatile flow and atherosclerosis in the human carotid bifurcation. Positive correlation between plaque location and low oscillating shear stress. *Ather.*, Vol. 3, p. 293-302.
- Ku, D.N. (1997). Blood Flow in Arteries. *Annu. Rev. Fluid. Mech.*, Vol. 29, p. 399-434.
- Kvitting, J.E., Ebbers, T., Wigstrom, L., Engvall, J., Olin, C.L., Bolger, A.F. (2004). Flow Patterns in the Aortic Root and the Aorta Studied with Time-Resolved, 3-Dimensional, Phase-Contrast Magnetic Resonance Imaging: Implications for Aortic Valve-Sparing Surgery. *J. Thor. Cardio. Surg.*, Vol. 127, p. 1602-1607.
- Lee, J.S. and Fung, Y.C. (1970). Flow in Locally Constricted Tubes at Low Reynolds Numbers. *J. Appl. Mech.*, Vol. 37, p. 9-16.
- Levy, B., Targett, R.C., Bardou, A., Mcilroy, M.B. (1985). Quantitative Ascending Aortic Doppler Blood Velocity in Normal Human Subjects. *Cardiovasc. Res.*, Vol. 19, p. 383-393.
- McDonald, D.A. (1974). Blood Flow in Arteries, Williams & Wilkens.
- Lighthill, M.J. (1975). Mathematical Biofluid-Dynamics. Philadelphia: Soc. Ind. Appl. Math. p. 281.

- Low, M., Perktold, K., Raunig, R. (1993). Hemodynamics in Rigid and Distensible Saccular Aneurysms: a Numerical Study of Pulsatile Flow Characteristics. *Biorheol.*, Vol. 30, p. 287-298.
- Middleman, S. (1972). Transport Phenomena in the Cardiovascular System. p. 5. John Wiley and Sons.
- Milner, J.S., Moore, J.A., Rutt, B.K., Steinman, D.A. (1998). Hemodynamics of Human Carotid Artery Bifurcations: Computational Studies with Models Reconstructed from Magnetic Resonance Imaging of Normal Subjects. *Jour. Vasc. Surg.* Vol. 28, p. 143-156.
- Moore J.A., Steinman D.A., Ethier C.R. (1998). Computational Blood Flow Modeling: Errors Associated with Reconstructing Finite Element Models from Magnetic Resonance Images. *J. Biomech.* Vol. 31, p. 179-184.
- Moore, J.A., Rutt, B.K., Karlik, S.J., Yin, K., Ethier, C.R. (1999). Computational Blood Flow Modeling Based on *In Vivo* Measurements. *Ann. Biomed. Eng.*, Vol. 27, p. 627-640.
- Moore, J.A., Steinman, D.A., Holdsworth, D.W., Ethier, C.R. (1999). Accuracy of Computational Hemodynamics in Complex Arterial Geometries Reconstructed from Magnetic Resonance Imaging. *Ann. Biomed. Eng.*, Vol. 27, p. 32-41.
- Moore, J.E., Xu, C., Glagov, S., Zarins, C.K., and Ku, D.N. (1994). Fluid Wall Shear Stress Measurements in a Model of the Human Abdominal Aorta: Oscillatory Behavior and Relationship to Atherosclerosis. *Ather.*, Vol. 110, p. 225-240.
- Myers, J.G., Moore, J.A., Ojha, M., Johnston, K.W., Ethier, C.R. (2001) Factors Influencing Blood Flow Patterns in the Human Right Coronary Artery. *Ann. Biomed. Eng.*, Vol. 29, p. 109-120.
- Nakamura, M., Sugiyama, W., Haruna, M. (1993). An Experiment on the Pulsatile Flow at Transitional Reynolds Numbers--The Fluid Dynamical Meaning of the Blood Flow Parameters in the Aorta. *J. Biomech. Eng.*, Vol. 115, p. 412-417.
- Naruse, T., and Tanishita, K. (1996). Large Curvature Effect on Pulsatile Flow in a Curved Tube. *J. Biomech. Eng.*, Vol. 118, p. 333-340.
- Nerem, R.M. (1992). Vascular Fluid Mechanics, the Arterial Wall, and Atherosclerosis. *J. Biomech. Eng.*, Vol. 114, p. 274-282.

- Pedley, T.J. (1980). *The Fluid Mechanics of Large Blood Vessels*, Cambridge UK: Cambridge, University Press.
- Perktold, K., Rappitsch, G. (1995). Computer Simulation of Local Blood Flow and Vessel Mechanics in a Compliant Carotic Artery Bifurcation Model. *Jour. Biomech.*, Vol. 28, p. 845-856.
- Perktold, K., Prosi, M., Leuprecht, A., Ding, Z., Friedman, M.H. (2001). Curvature Effects on Bifurcating Coronary Artery Flow. 2001 Bioengineering Conference, BED-Vol. 50, p. 69-70, ASME, New York.
- Poutanen T., Tikanoja T., Sairanen H., Jokinen E. (2003). Normal Aortic Dimensions and Flow in 168 Children and Young Adults. *Cli. Physiol. Fun. Imag.*, Vol. 23, p. 224-229.
- Prakash S., Ethier C.R. (2001). Requirements for Mesh Resolution in 3D Computational Hemodynamics. *J. Biomech. Eng.* Vol. 123, p. 134-144.
- Qiu, Y., and Tarbell, J.M. (2000). Numerical Simulation of Pulsatile Flow in a Compliant Curved Tube Model of a Coronary Artery. *J. Biomech. Eng.*, Vol. 122, p. 77-85.
- Resnick, N., Gimbrone, M.A. Jr. (1995). Hemodynamic Forces are Complex Regulators of Endothelial Gene Expression. *FASEB J.*, Vol. 9, p. 874-882.
- Roache, P. J. (1998). *Verification and Validation in Computational Science and Engineering*, Hermosa Publishers, Albuquerque, NM.
- Rodkiewicz, C.M. (1975). Localization of Early Atherosclerotic Lesions in the Aortic Arch in the Light of Fluid Flow. *J. Biomech.*, Vol. 8, p. 149-156.
- Ross, R. (1995) Cell Biology of Atherosclerosis. *Ann. Rev. Physiol.*, Vol. 57, p. 791-804.
- Sabbah, H.H., Khaja, F., Hawkins, E.T., Brymer, J.F., McFarland, T.M., Van der Bel-Kahn, J., Stein, P.D. (1986). Relation of Atherosclerosis to Arterial Wall Shear in the Left Anterior Descending Coronary Artery of man. *Am. Heart J.*, Vol. 112, p. 453-458.
- Shahcheragi, N., Dwyer, H.A., Cheer, A.Y., Barakat, A.I., Rutaganira, T. (2002). Unsteady and Three-Dimensional Simulation of Blood Flow in the Human Aortic Arch. *J. Biomech. Eng.*, Vol. 124, p. 378-387.
- Singh, M.P., 1974. Entry Flow in a Curved Pipe. *J. Fluid. Mech.*, Vol. 65, p. 517-539.

- Stein, P.D., Sabbah, H.N. (1976). Turbulent Blood Flow in the Ascending Aorta of Humans with Normal and Diseased Aortic Valves. *Circ Res.*, Vol. 39, p. 58-65.
- Sun, H., Kuban, B.D., Schmalbrock, P., Friedman, M.H. (1994). Measurement of the Geometric Parameters of the Aortic Bifurcation from Magnetic Resonance Images. *Ann. Biomed. Eng.*, Vol. 22, p. 229-239.
- Taylor, C.A., Hughes, T.J.R., Zarins, C.K. (1998). Finite Element Modeling of Three-Dimensional Pulsatile Flow in the Abdominal Aorta: Relevance to Atherosclerosis. *Ann. Biomed. Eng.*, Vol. 26, p. 975-987.
- Traub, O., and Berk, B.C. (1998). Laminar Shear Stress-Mechanisms by which Endothelial Cells Transduce and Atheroprotective Force. *Arterioscl. Thromb. Vasc. Biol.*, Vol. 18, p. 123-124.
- Tsutsui, H., Yamagishi, M., Uematsu, M., Suyama, K., Nakatani, S., Yasumura, Y., Asanuma, T., Miyatake, K. (1998). Intravascular Ultrasound Evaluation of Plaque Distribution at Curved Coronary Segments. *Am. J. Cardiol.*, Vol. 81, p. 977-981.
- Van Dam I., Heringa, A., De Boo T. (1987). Reference Values for Pulsed Doppler Signals from the Blood Flow on Both Sides of the Aortic Valve. *Eur. Heart J.*, Vol. 8, p. 1221-1228.
- Wesolowski, S.A., Fries, C.C., Sabini, A.M., and Sawyer, P.N. (1965). Turbulence, Intimal Injury, and Atherosclerosis. In *Biophysical Mechanisms in Vascular Homeostasis and Intravascular Thrombosis*, p. 147-157, Appleton-Century-Crofts, New York.
- White, F.M., 1979. *Viscous Fluid Flow*, McGraw-Hill, New York.
- Wislon N., Goldberg S.J., Dickinson D.F., Scott O. (1985). Normal Intracardiac and Great Artery Blood Velocity Measurements by Pulsed Doppler Echocardiography. *Br. Heart J.*, Vol. 53, p. 451-458.
- Womersley, J.R. (1955). Method for the Calculation of Velocity, Rate of Flow and Viscous Drag in Arteries when their Pressure Gradient is known. *J. Physiol.*, Vol. 127, p. 553-563.
- Yamagushi, R. (1999). Flow Structure and Variation of Wall Shear Stress in Asymmetrical Arterial Branch. *J. Fluids and Struct.* Vol. 13, p. 429-442.
- Yao, L.S. and Berge, S.A. (1975). Entry Flow in a Curved Pipe. *J. Fluid. Mech.*, Vol. 67, p. 177-196.

- Yearwood, T.L., and Chandran, K.B. (1984). Physiological Pulsatile Flow Experiments in a Model of the Human Aortic Arch. *J. Biomech.*, Vol. 15, p. 683-704.
- Zarins, C.K., Giddens, D.P., Bharadvaj, B.K., Sottiurai, V.S., Mabon, R.F., and Glagov, S. (1983). Quantitative Correlation of Plaque Localization with Flow Velocity Profiles and Wall Shear Stress. *Circ. Res.*, Vol. 53, p. 502-514.
- Zhao, S.Z., Xu, X.Y., Hughes, A.D., Thom, S.A., Stanton, A.V., Ariff, B., Long, Q. (2000). Blood Flow and Vessel Mechanics in a Physiologically Realistic Model of a Human Carotid Arterial Bifurcation. *Jour. Biomech.* Vol. 33, p. 975-984.